In-vivo localisation of human acetylcholinesterase-derived species in a β-sheet conformation at the core of Alzheimer's disease senile plaques

Létitia Jean[1], Stephen Brimijoin[2] and David J. Vaux[1#]

[1]Sir William Dunn School of Pathology, University of Oxford, Oxford OX1 3RE, UK
[2]Mayo Clinic, Department of Molecular Pharmacology and Experimental Therapeutics, 200 First Street SW, Rochester, MN 55905, USA

Running Title: Conformation of hAChE-S species in senile plaques

[#] To whom correspondence may be addressed: David J. Vaux, Sir William Dunn School of Pathology, University of Oxford, South Parks Road, Oxford OX1 3RE, UK, Tel.: 0044-1865-275-544; Fax: 0044-1865-275-591; E-mail: david.vaux@path.ox.ac.uk

Key words: Alzheimer's disease, acetylcholinesterase, oligomerisation domain, proteolysis, brain, transgenic mice, Aβ, β-sheet conformation, senile plaques, seeding

ABSTRACT

Many neurodegenerative diseases are characterized by amyloid deposition. In Alzheimer's disease (AD), amyloid-β-peptides (Aβ) accumulate extracellularly in senile plaques. The AD amyloid cascade hypothesis proposes that Aβ production or reduced clearance leads to toxicity. In contrast, the cholinergic hypothesis argues for a specific pathology of brain cholinergic pathways. However, neither hypothesis in isolation explains the pattern of AD pathogenesis. Evidence suggests that a connection exists: the synaptic form of human acetylcholinesterase (hAChE-S) associates with plaques in AD brains; among hAChE variants, only hAChE-S enhances Aβ fibrilisation *in-vitro,* and Aβ deposition and toxicity *in-vivo*. Only hAChE-S contains an amphiphilic C-terminal domain (T40, $\mathrm{AChE}_{575\text{-}614}$), with $\mathrm{AChE}_{586\text{-}599}$ homologous to Aβ and forming amyloid fibrils, which implicates T40 in AD pathology. We previously showed that the amyloid scavenger, insulin degrading enzyme (IDE), generates T40-derived amyloidogenic species that, as a peptide mixture, seed Aβ fibrilisation. Here, we characterised 11 peptides from a T40-IDE digest for β-sheet conformation, surfactant activity, fibrilisation, and seeding capability. We found residues important for amyloidogenicity and raised polyclonal antibodies against the most amyloidogenic peptide. These new antisera, alongside other specific antibodies, labeled sections from control, hAChE-S, hAPPswe, and hAChE-S/hAPPswe transgenic mice. We saw hAChE-S β-sheet species co-localising with Aβ in mature plaque cores, surrounded by hAChE-S α-helical species. This provides the first *in-vivo* evidence of the conformation of hAChE-S species within plaques. The results may yield insights to explain hAChE-S role in Aβ deposition and aggregation, as amyloidogenic hAChE-S β-sheet species might seed Aβ aggregation.

A rising number of pathologies of great public health concern (e.g. Alzheimer's disease, AD, and type II diabetes) result from polypeptide misfolding, ordered aggregation and aggregate deposition, known as amyloids (1). Although amyloids originate from distinct polypeptides and share no sequence homology, they have similar properties (e.g. cross β-sheet structure) (2,3). Amyloidogenesis is driven by properties of the sequence backbone and specific side-chain interactions (4-7). AD hallmarks are extracellular deposits of amyloid-β-peptides (Aβ) in senile plaques and intracellular deposition of hyper-phosphorylated Tau in neurofibrillary tangles (NFT) (8). Aβ originates from sequential proteolysis of human amyloid precursor protein (hAPP). Various mutations in hAPP lead to hereditary AD forms (e.g. Swedish mutation, hAPPswe). The amyloid cascade hypothesis of AD proposes that Aβ is ultimately responsible for pathology during which increased Aβ production or reduced clearance leads to toxicity (1). Although elevated plaque burden is the histological criterion for AD diagnosis, only the level of soluble Aβ found in cerebrospinal fluid correlates with disease severity.

Senile plaques in AD brain also contain ‘secondary’ molecules, among which is the synaptic form of human acetylcholinesterase (hAChE-S). The cholinergic hypothesis sees AD as a specific pathology of brain cholinergic pathways: acetylcholine-mediated neurotransmission is selectively and severely impaired or lost, basal forebrain cholinergic neurons are the most affected, normal hAChE-S hippocampal and cortical fibre networks are severely reduced, and hAChE-S inhibition for one year with donepezil in suspected prodromal AD patients decreases the rate of hippocampal atrophy by 45% (9-17). Unfortunately, neither the amyloid cascade nor the cholinergic hypothesis alone explains the full extent of AD pathogenesis. Evidence of a connection includes: altered hAChE-S (catalytically, oligomerisation and glycosylation) is associated with AD plaques and tangles, hAChE-S enhances Aβ fibrilisation *in-vitro* (leading to stable complexes that alter its catalytic activity) and Aβ toxicity *ex-vivo* and *in-vivo,* and mice expressing both hAPPswe and hAChE-S show earlier disease onset than single transgenic mice (18-25). The spread of senile plaque-containing hAChE-S beyond brain areas rich in cholinergic innervation also suggests that hAChE-S role in plaque formation goes beyond cholinergic activity.

Several hAChE variants result from alternative splicing (hAChE-S and hAChE-R, for readthrough), or alternative promoter usage (N-AChE-S and N-AChE-R, with an extended N-terminus) (26). In contrast to the synaptic variants, the readthrough variants delay Aβ fibrilisation and tau hyper phosphorylation, and inversely affect plaque burden in transgenic mice (hAPPswe-hAChE-R vs hAPPswe-hAChE-S)(21). The two variants only differ in their C-terminal domains, with only hAChE-S containing the amphiphilic 40 residue C-terminal domain (T40, AChE$_{575-614}$), implicating T40 in AD pathology (27). T40’s classic role is to mediate oligomerisation to form a variety of hAChE-S isoforms (e.g. soluble and amphiphilic, membrane bound or anchored to the extracellular matrix). Intact, T40 is non-amyloidogenic, α-helical and does not promote Aβ assembly (28,29). T40 has a region, AChE$_{586-599}$, with shared homology to Aβ, which as a peptide under physiological conditions, adopts β-sheet conformation, is amyloidogenic and promotes Aβ nucleation (28,30,31). *In-vitro* T40-derived amyloid species are generated by insulin-degrading enzyme (IDE), a protease implicated in Aβ processing and genetically linked to AD. IDE-T40 peptides adopt β-structures, are amyloidogenic and promote Aβ assembly (28). C-terminal T40 proteolysis of hydrophilic monomers and tetramers of bovine AChE-S occurs *in-vivo* (32). Also, naturally occurring soluble monomeric G1 AChE from foetal bovine serum, but not the tetrameric G4 form, lacks the T40 domain (33). These studies suggest that *in-vivo* T40 is vulnerable to proteolysis even in tetramers and cleaved T40 from G1 AChE can be further digested to generate amyloidogenic species.

Amyloidogenesis is a nucleation-dependent polymerisation with an energetically unfavourable lag-phase, an elongation phase (nuclei extension by monomer addition), and a plateau phase when fibril extension ends (3). To promote nucleation, initial triggers may be required. For example, during seeding, homologous or heterologous amyloidogenic species provide a conformationally competent template to accelerate initial misfolding and formation of early assembly intermediates, including toxic oligomers (3). *In-vitro* and *in-vivo* seeding occurs in various amyloid systems, including Aβ (34-36). Plaque-associated hAChE-S may promote heterologous seeding of Aβ, which would accelerate toxic oligomer formation and might result in stable Aβ-hAChE-S hetero-complexes (19). This seeding hypothesis may represent a previously undescribed pathological trigger for more severe Aβ pathology during AD, in which Aβ abundance is not the only driving factor. Thus, detailed dissections of the protagonists involved, including their recruitment, formation and participation in amyloidogenesis, should provide invaluable insights for targeting and controlling diseases involving toxic protein aggregation and deposition.

Here we investigated the *in-vivo* implication of hAChE-S in AD pathology, using a double transgenic mice model for hAChE-S/hAPPswe (Tg2576 background, APP_{695} isoform)(37). In contrast to hAPPswe single transgenic mice, these mice develop more numerous, frequent and early amyloid plaques (6 months), which contain $A\beta_{1\text{-}40}$, $A\beta_{1\text{-}42}$, markers of activated microglia and reactive astrocytes, and hAChE-S, as do natural AD amyloid deposits (37). The extent of amyloid burden was also tightly correlated with memory impairment, more so than in the hAPPswe single transgenic mice (18). In contrast to transgenic mice with various forms of hAPP, which only address Aβ-related pathology, the presence of the hAChE-S transgene also confirms changes resulting in an imbalance of cholinergic function and neurotransmission. Indeed, overexpression of hAChE-S in transgenic mice triggers a progressive decline in spatial learning and memory, cessation of dendritic branching, reduced number of spines in cortical neurons, and enhanced high-affinity choline uptake, all of these being hallmarks of cholinergic malfunction and characteristics reported in senile dementia (38,39). Opposite effects were observed in mice transgenic for hAChE-R (40).

This study used synthetic peptides corresponding to products of IDE proteolysis on hAChE-S T40 to fully characterise their potential in terms of β-sheet propensity and conformation, surfactant activity, fibrilisation, co-fibrilisation and seeding of Aβ. We established the importance of sequences or residues underlying plaque assembly and we selected the most amyloidogenic peptide for raising specific antibodies. The new antisera were characterised for specificity and used with other specific antibodies to immune-label coronal brain sections from 12-month old wild-type, hAChE-S single transgenic, hAPPswe single transgenic (Tg2576, APP_{695} isoform), and hAChE-S/hAPPswe double transgenic mice. Mature plaques in cerebral cortex contained hAChE-S and Aβ, as in AD. Importantly, hAChE-S β-sheet species were detected in plaque cores, surrounded by α-helical forms. Plaque hAChE-S β-sheet species co-localised with fibrilar amyloid material and Aβ. These findings provide the first *in-vivo* evidence of hAChE-S conformation in senile plaques.

RESULTS

We previously established that IDE proteolysis of T40 generates amyloid species seeding Aβ fibrilisation (28). Now we have characterised a set of individual synthetic peptides identified from a T40-IDE digest, rather than as a peptide mixture. Two new antisera were generated by immunisation with the 'best' amyloidogenic T40-IDE peptide, to use along with other specific antibodies to label brain sections of control mice, hAChE-S, hAPPswe and hAChE-S/hAPPswe transgenic mice.

Key residues for β-sheet propensity and conformation- β-sheet formation is one driver of amyloidosis in AD. It is important to assess the propensity of T40-IDE peptides for conversion to non-native (hidden) β-strands. We used the algorithm of Yoon and Welsh, who predicted minimal amyloidogenic regions for α-synuclein and Aβ and showed $AChE_{586\text{-}599}$ as an hAChE-S region with high β-strand propensity (31). Previously, we identified YMVH as the $AChE_{586\text{-}599}$ sequence with strongest propensity for β-strand conversion, and W_{591}, Y_{594}, M_{595}, V_{596}, W_{598} as crucial to maintain high β-strand propensity along the entire sequence (28). Applied to T40-IDE peptides, the algorithm revealed that β-strand conversion depends on surrounding sequences, and identified two regions, WKAEFHR and SYMVHWK (Fig. 1). W_{591} and S_{592} were predicted as random coils, unlike their configuration in the $AChE_{586\text{-}599}$ context. It was also evident that T40 N-terminus (DTLDEAERQ) and C-terminus (NQFD) have propensities for both random coil and α-helix, and that H_{589} has a negative effect on the following RWSS. The two peptides with the strongest predicted propensity for β-strand conversion are $AChE_{590\text{-}598}$ (RWSSYMVHW) and $AChE_{594\text{-}598}$ (YMVHW).

We further analysed the T40-IDE peptides using three other algorithms, which confirmed the findings from the Yoon and Welsh algorithm (Fig. S1-S3). CamSol, which predicts protein solubility and generic aggregation propensity, identified SYMVHWK as being poorly soluble, followed by KAEFHR, the T40 N- and C-termini being highly soluble, and H$_{589}$-R$_{590}$ to have negative effects on the following WSS (Fig. S1) (41). TANGO predicts β-sheet aggregation, percentage occupancy of β-sheet aggregation, β-sheet and α-helical conformations (42). TANGO identified AEFHR and YMVHW as having β-sheet aggregation propensity, AChE$_{585-597}$ and AChE$_{590-598}$ (the immunisation peptide used later in the study) as having the two highest aggregation propensity, and H$_{589}$ along with T40 N-terminus as having a negative impact (Fig. S2). WALTZ, which identifies protein motifs that nucleate amyloid fibre formation, recognised RWSSYMV as having amyloid propensity (Fig. S3) (43).

Next we used far-UV CD to follow conformational changes of T40-IDE peptides before (acidic pH) or during aggregation (neutral pH). In previous studies, AChE$_{586-599}$ was random coil when non-aggregated, but β-sheet on neutralisation. F$_{588}$, W$_{591}$, S$_{592}$, S$_{593}$, Y$_{594}$, M$_{595}$, V$_{596}$, W$_{598}$ were all important in the conformational transition (28,30). Fig. 2 and S4 represent and summarise the conformational changes. At acidic pH, all peptides but AChE$_{582-594}$, had some random coil conformation (negative ellipticity ~200 nm or less). All peptides but AChE$_{575-593}$ (α-helical, double negative ellipticity minima ~208 and 220 nm) had partial β structures, with the majority having a dominant β-sheet conformation (double negative ellipticity minima at 200 and 215 nm). After 24 hrs neutralisation, three peptides still showed dominant random coil conformations: AChE$_{584-603}$, AChE$_{589-599}$, AChE$_{594-598}$. Another, AChE$_{575-593}$ remained dominantly α-helical, and AChE$_{589-598}$ underwent a conformational change from a dominant random coil to dominantly α-helical. In contrast, AChE$_{590-598}$ only adopted β-sheet conformation, rather than a mixed β-sheet/random coil. In term of adoption and/or conformational change to β-sheet conformation, these results indicate negative effects of the T40 N- and C-termini (DTLDEAERQ in AChE$_{575-593}$, and NQFD in AChE$_{584-603}$), and the detrimental effect of H$_{589}$ (AChE$_{589-598}$/AChE$_{589-599}$ versus AChE$_{590-598}$). We also found that R$_{582}$Q$_{583}$ are important for adoption of a partial β-turn rather than a partial random coil conformation (AChE$_{582-594}$ versus AChE$_{584-594}$).

A further question was if non-dominant β-sheet T40-IDE peptides would adopt a dominant β-sheet conformations at high concentrations or if membrane-mimicking SDS was present (Fig. 3). For AChE$_{584-594}$ (WKAEFHRWSSY), double concentration caused a transition from weak dual random-coil/β-sheet to dominant β-sheet (Fig. 3*A*). With SDS present, AChE$_{584-594}$ remained a mixed random coil/β-sheet (Fig. 3*B*). For AChE$_{589-598}$ (HRWSSYMVHW), which was in β-sheet-β-turn-random coil conformation after 10 min neutralisation, double concentration converted it to a strong dominant β-sheet conformation (Fig. 3*A*). In the presence of SDS, AChE$_{594-598}$ (YMVHW) converted from a dominant random coil to a dominant β-sheet (Fig. 3*B*). These results highlight importance of local peptide context. Indeed changing concentration or presence of local membranes are likely to influence conformation, and in turn amyloidogenesis. Order of β-sheet competence: AChE$_{590-598}$> AChE$_{582-594}$>AChE$_{585-593}$= AChE$_{584-594}$>AChE$_{591-601}$.

Key fibrilisation residues- To study fibrilisation kinetics of T40-IDE peptides, we used a classical amyloid dye, ThT, that intercalates in β-sheet amyloid structures and we assessed changes in its fluorescence emission (44). Shaking was used to accelerate fibrilisation, and was necessary for some peptides. AChE$_{586-599}$ was a positive control with well-established fibrilisation kinetics (28). AChE$_{586-599}$ fibrilisation showed biphasic behaviour: first, rapid assembly (<1 hr) followed by a short plateau and decreased ThT signal, and a second slower assembly (>5 hrs) followed by the same effects (Fig. 4*A*). This behaviour was previously shown to be triggered by assay shaking and thought to arise from susceptibility to breakage by shear forces, or increasing surface area and peptide recruitment (28). Also as previously found, the decay of ThT signal after plateau suggested that AChE$_{586-599}$ assembly was not stable under these conditions.

At 100 μM, only six peptides fibrilised, all (except AChE$_{585-597}$) with significantly longer nucleation (lag phase), leading to a much lower plateau than AChE$_{586-599}$ (Fig. 4*A*-*C*). For each except AChE$_{585-597}$, the assembly was stable and plateau ThT signals did not decay. The order of fibrilisation competence was: AChE$_{585-597}$>AChE$_{590-598}$>AChE$_{589-598}$>AChE$_{591-}$

$_{601}$>AChE$_{584-594}$>AChE$_{584-603}$. At 200 μM, the lag phase of the poorest peptide, AChE$_{584-594}$, was significantly reduced (~13.3 to ~2.6 hrs) and its plateau height more than doubled (1155 to 2699 a.u.)(Fig. 4*D*). At 200 μM, AChE$_{589-599}$ fibrilised but slowly and weakly (lag phase of 16.7 hrs and plateau height of 333 a.u.)(Fig. 4*D*).

We then examined the aggregation status of the fibrilising T40/IDE peptides by electron microscopy (Fig. 5). All fibrilising peptides were clearly aggregated into dense meshworks of fibrils (top panel for each peptide), with individual typical amyloid fibrils clearly identifiable (lower panel for each peptide).

Most fibrilising peptides adopted a degree of β-sheet conformation after neutralisation. The non-fibrilising AChE$_{582-594}$ showed both a β-sheet and β-turn conformation, the latter possibly hindering amyloid cross β-sheet formation. Similarly, the non-fibrilising AChE$_{589-599}$ and AChE$_{594-598}$ mainly adopted a random coil conformation but also had some β-sheet and β-turn. These results indicate the importance of YMVH as only T40-IDE peptides containing it fibrilised (except AChE$_{584-594}$).

AChE$_{590-598}$ and AChE$_{585-597}$ are seeds for fibrilisation of other AChE-derived peptides-AChE$_{585-597}$ (KAEFHRWSSYMVH) and AChE$_{590-598}$ (RWSSYMVHW) were the two best in terms of fibrilisation. As these two peptides were unlikely to fibrilise by themselves *in-vivo*, we investigated whether the monomers could interact with other T40-IDE peptides and AChE$_{586-599}$ monomers to enhance fibrilisation. Co-fibrilisation of T40-IDE peptide monomers with 50 μM of AChE$_{590-598}$ or AChE$_{585-597}$ monomers, triggered fibrilisation of T40-IDE peptides that would not fibrilise by themselves at either 50 or 100 μM (AChE$_{575-593}$, AChE$_{582-594}$, AChE$_{585-593}$, AChE$_{589-599}$, AChE$_{594-598}$), or at 50 μM (AChE$_{584-594}$)(Fig. 6). In contrast to AChE$_{585-597}$, AChE$_{590-598}$ also shortened the lag phase and increased the plateau height of AChE$_{586-599}$.

Key residues for surface activity-Many amyloids are amphiphilic and surface active, allowing efficient adsorption to hydrophobic-hydrophilic interfaces (HHI) (45-52). HHIs act as fibrilisation catalysts due to a concentrating effect and promotion of peptide chain alignments that favour β-sheet formation. This is important because *in-vivo* HHIs, cellular membranes (phospholipid bilayers with a hydrophilic outer layer and a hydrophobic core), are structurally and functionally damaged by amyloids (1,8). Since surface activity plays a major role in amyloid toxicity, it was important to assess surface activity of the T40-IDE peptides. We used a previously described technique based on an off-axial light beam to measure the meniscus lensing effect (47). Normalising the apparent optical density at the offset using optical density measured on the central axis (ΔOD) gave values that correlated strongly and inversely with surface tension (R>0.97) (47,53).

AChE$_{586-599}$ surfactant activity was previously found highly pH dependent, with little surface activity at acidic pH, likely due to histidine protonation (47). Hence we began testing surface activity of the T40-IDE peptides by measuring differential absorbance (ΔOD) at acidic and neutral pH (Fig. 7*A* and *C*). AChE$_{584-603}$, AChE$_{575-593}$ and AChE$_{585-593}$ had weaker surface activity (smaller ΔOD) than AChE$_{586-599}$, and AChE$_{594-598}$ surface activity was similar to that of AChE$_{586-599}$. All other peptides were more surface-active than AChE$_{586-599}$ (higher ΔOD) after 2 min at neutral pH.

Assessing temporal patterns of surfactant activity after neutralisation, most peptides were not stably surface active (Fig. 7*B* and *C*) and their activity dropped readily. This suggests that they quickly adsorbed at the air-water interface after neutralisation, but subsequent partial decreases in surface activity may reflect conformational changes at the air-water interface to reduce effects on surface energy. In contrast, surface activities of AChE$_{586-599}$, AChE$_{584-603}$, AChE$_{590-598}$ and AChE$_{591-601}$ were stable, suggesting these peptides remained associated with the air-water interface all along. Orders of competent surface activity were as follows: AChE$_{590-598}$>AChE$_{591-601}$=AChE$_{582-594}$>AChE$_{585-597}$>AChE$_{584-594}$=AChE$_{589-599}$>AChE$_{589-598}$>AChE$_{594-598}$.

T40-IDE peptides act as heterologous seeds to promote Aβ fibrilisation-We examined the ability of the T40-IDE peptides to promote Aβ fibrilisation. We used 2 μM peptide seeds, not monomers, to assess heterologous seeding of 15 μM Aβ. These conditions were identical to Diamant *et al.* and Jean *et al.*, for direct comparison with their previous studies on hAChE effects on Aβ fibrilogenesis (28,29).

Seed concentration is the initial monomer concentration used to prepare them. By themselves they did not contribute to ThT signals in test wells, as they did not generate signals over background (not shown). Moreover, seed-ThT values (no Aβ) were subtracted from all test assays with Aβ. Without seeds, Aβ showed a plateau height of ~1095 a.u. after a ~43.4 hr lag and an elongation rate of ~ 89.7 a.u./hr (Fig. 8 and Fig. S5). The positive control, 2 μM $AChE_{586-599}$ seeds, reduced Aβ lag phase, 1.4 fold, and its plateau height, 1.2 fold (Fig. 8*A* and *C*). Similar seeding activity for $AChE_{586-599}$ seeds was previously observed (28). With the exception of $AChE_{584-603}$ seeds, all other T40-IDE seeds reduced Aβ lag phase significantly, with $AChE_{589-599}$ being most effective. The seeds of $AChE_{584-603}$, $AChE_{585-597}$, $AChE_{584-594}$, $AChE_{585-593}$, $AChE_{590-598}$ and $AChE_{594-598}$ accelerated Aβ elongation rate (from 1.1 to 1.3 fold), with $AChE_{584-603}$ seeds being the most effective (Fig. 8*B*). All peptide seeds, except those of $AChE_{584-603}$, increased Aβ plateau height (from 1.1 to 1.2 fold), with $AChE_{585-593}$ being most effective (Fig. 8*C*).

Specificity of new antisera against $AChE_{590-598}$-After characterising T40-IDE peptides, RWSSYMVHW ($AChE_{590-598}$) emerged as the most amyloidogenic. It had the strongest propensity for conversion to β-strand, strongest surface activity, the best at adopting β-sheet conformation, was second best at fibrilising, and fair at Aβ seeding. Therefore, two rabbit polyclonal antibodies, 3313 and 3314, were produced using C-Ahx-$AChE_{590-598}$-acid coupled at the N-terminus to KLH as an antigen. Specificity of these antibodies was tested by immuno-blot using T40-IDE peptides (monomers or seeds), T40, hAChE-S and Aβ (monomers and fibrils) as antigens, and were compared to that of Mab 105A, specific to $AChE_{586-599}$ in a β-sheet conformation (Fig. 9). Importantly, neither Mab 105A nor polyclonal 3313 and 3314 cross-reacted with Aβ monomers or fibrils, despite using an amount of Aβ fibrils far above that found *in-vivo* (Fig. 9) (54-56). The extremely low reactivity against Aβ fibrils seen in the immuno-blots with 3313 and 3314 was a non-specific cross-reactivity by the polyclonal secondary antibodies anti-rabbit (probably due to the inherent stickiness of fibrils) (Fig. 9*B inset*).

For 105A, its previously published specificity, established by scanning alanine mutant recognition, for $AChE_{586-599}$ was confirmed in two ways (30). Firstly, 105A epitope was mapped by using 105A as a bait to select, from a large random peptide phage library, clones expressing short seven residue peptides bearing its epitope (Supplementary experimental procedures). With this technique, the previously mapped epitope specificity of 105A was confirmed to be AxFHR (Fig. S6). Secondly, the recognition of $AChE_{586-599}$ was the strongest by slot-blot (Fig. 9). 105A also recognised $AChE_{584-603}$ monomers and hAChE-S, but the signal was much fainter. Importantly, α-helical T40 was not recognised, confirming 105A specificity for β-sheet conformations. Polyclonal 3313 reacted strongly against monomers of the immunisation peptide and of $AChE_{584-603}$. Significant reactivity was also detected for seeds of the immunisation peptide and of $AChE_{585-597}$, and T40. Low level reactivity was observed for $AChE_{585-597}$/$AChE_{589-598}$ monomers, seeds of $AChE_{584-603}$/$AChE_{585-597}$/$AChE_{584-594}$, and hAChE-S. Polyclonal 3314 reacted strongly against $AChE_{584-603}$ monomers and $AChE_{585-597}$ seeds. Significant reactivity was also detected for seeds of $AChE_{584-603}$/$AChE_{589-598}$/$AChE_{590-598}$, $AChE_{586-599}$ and hAChE-S. Low level reactivity was observed for monomers of $AChE_{575-593}$/$AChE_{585-597}$, seeds of $AChE_{584-594}$/$AChE_{586-599}$/immunisation peptide, and T40. The specificity of 3313 and 3314 is explained by the fact that most T40-IDE peptides either adopted a β-sheet conformation or fibrilised. Exceptions were fibrilising $AChE_{591-601}$ that is not recognised, and non-fibrilising and random coil $AChE_{575-593}$ that is weakly recognised by 3314. To summarise, 3313 and 3314 share some similar specificities for peptides that fibrilise, although the recognition level for individual peptides vary. However, 3313 and 3314 specificities differ from 105A. The strong target all three antibodies share is for $AChE_{584-603}$ monomers, which contains both the 105A epitope (FHR) and the full sequence of immunisation peptide $AChE_{590-598}$ for 3313 and 3314 (30).

Distribution of Aβ, hAChE-S, hAChE-S related species and ThS positive plaques-We next performed immunolabelling of coronal sections of brain from 12 month old control, hAChE-S or hAPPswe single transgenic mice (Tg2576, APP_{695} isoform), and hAChE-

S/hAPPswe double transgenic mice to probe for presence of hAChE-S derived peptides. To visualise hAChE-S we used mouse Mab HR2 anti-cerebellar hAChE-S and rabbit polyclonal KD69 anti-α helical T40 (which recognises globular intact hAChE-S but also α-helical T40 in isolation) (30). To visualise Aβ species, we used mouse specific Mab Bam10 anti-Aβ (first 12 residues). To detect β-sheet amyloid species, ThS was used. To detect hAChE-S species in a β-sheet conformation, we used specific mouse Mab 105A anti-AChE$_{586-599}$ (30). To detect hAChE-S species derived from cleavage of T40, we used our two new rabbit polyclonal 3313 and 3314.

ThS and all antibodies were negative on sections from wild-type mice (Fig. 10*A*). The only reactivity in sections from hAChE-S mice was with HR2 and KD69 recognising globular hAChE-S, as expected since such mice do not develop amyloid plaques (Fig. 10*B*). In sections of hAPPswe mice, numerous mature plaques could be identified by single antibody labelling (Fig. 11*A*, *left column*). Some of these plaques clearly contained Aβ species (labelled with Bam10), but also AChE-S (labelled with HR2) and AChE-S in β-sheet conformation (labelled with 105A, black arrowheads). Some plaques labelled only with anti-AChE-S antibodies, either anti-intact or anti-AChE-S domains (examples marked by blue arrowheads). There was clearly some peroxidase activity on sections incubated with KD69, 3313 and 3314. The brown colour was darker, and localised in more specific areas than the controls (no first antibody, only biotinylated secondary antibody, avidin-peroxidase and DAB). But no plaques were obvious. Similarly, numerous mature plaques were identified by single antibody labelling in sections of hAPPswe/hAChE mice (Fig. 11*A*, *right column*). Several Bam10-positive plaques were clearly bigger than in hAPPswe mice. ThS confirmed their amyloid nature (Fig. 11*B*). Labelling with avidin fluorescein reduced non-specific background but clearly raised specific signal above background in 3313 and 3314. Each antibody highlighted mature plaques in the same brain areas detected by peroxidase/DAB staining.

In single and double transgenic brain sections, plaques were mainly detected in the cerebral and olfactory cortices and a few in the olfactory bulb (e.g. ThS, Bam10 and 3314) (Fig. 11*A*, *B* and *C*). In the cerebral cortex section studied (rostral level), all sub-areas (motor, orbital and prelimbic) showed plaques, with stronger fluorescence in the motor sub-area with some reagent/antibodies (e.g. ThS, KD69, Bam10 and 3314). In the olfactory cortex (anterior olfactory nucleus), plaques were detected in all sub-areas. In the olfactory bulb (main and accessory), the plaques appeared more restricted to the granular layer.

When the area occupied by each fluorescent labelling, in the whole brain section of hAPPswe/hAChE double transgenic, was quantitated, it became evident that each individual antibody labelled only a small portion of the area labelled with ThS (Fig. 11*D*, *top and bottom graphs*). Indeed, KD69 labelling occupied an area only ~9.9% of that of ThS, Bam10 labelling 13.3%, 105A labelling 1.3%, 3313 labelling 2.8%, and 3314 labelling 25.4%. The same relationship was found when the overall intensity of the fluorescent labelling by each antibody was measured, with KD69 labelling intensity only ~8.9% that of ThS, Bam10 labelling 25%, 105A labelling 3.8%, 3313 labelling 3.8%, and 3314 labelling 20.3% (Fig. 11*D*, *middle and bottom graphs*). These results clearly suggest that Aβ and hAChE-S related species only represent a fraction of the overall amyloid burden.

hAChE-S related species in a β-sheet conformation are located in plaques and colocalise with Aβ-We subsequently addressed by double fluorescent labelling whether amyloid positive plaques contained hAChE-S of various kinds, including intact, truncated, α-helical or β-sheet. In the cerebral cortex of hAPPswe mice, mature amyloid plaques could be detected, which labelled with anti-Aβ Bam10 and ThS (Fig. 12). The Aβ species showed some degree of colocalisation with mouse AChE-S (HR2)(68.6% of Bam10 labelling overlapping with that of HR2, and 10.2% of HR2 labelling overlapping with that of Bam10) and mouse AChE-S species with α-helical T40 (KD69)(61.8% of Bam10 labelling overlapping with that of KD69, and 36.2% of KD69 labelling overlapping with that of Bam10), with mouse AChE-S surrounding the Aβ species (Fig. 12*A*). Human AChE T40 and mouse equivalent differ by only one amino acid conservative substitution, D$_{609}$ in human to E$_{609}$ in mouse. Therefore, K69 should recognise both human and mouse T40 sequences, as observed.

Moreover, the entire hAChE-S and mouse AChE-S amino acid sequences share 88.4% identity, with 71 substitutions among which 43 are conservative, 10 semi-conservative, and 18 non-conservative. Moreover, HR2 was also seen to cross-react with mouse AChE-S by immunofluorescence in mouse Neuro-2 neuroblastoma cells (GeneTex, http://www.genetex.com/ AChE-antibody-HR2; abcam, http://www. abcam.com/ acetyl-cholinesterase antibody-hr2-ab2803.html). Thus, it is not surprising that KD69 and HR2 recognise mouse AChE-S. 105A and 3313/3314 also labelled plaques (Fig. 12*B* and 13). 105 epitope ($F_{588}H_{589}R_{590}$) and 3313/3314 immunising peptide $AChE_{590-598}$ are identical between human and mouse. Since the *Ide* gene is conserved between human and mouse, it would be highly likely that mouse T40-IDE peptides would be generated from mouse AChE-S. 105A labelling of mouse AChE-S β-sheet species was found at the core of mature plaques, colocalising with Aβ (10.4% of Bam10 labelling overlapping with that of 105A, and 68.3% of 105A labelling overlapping with that of Bam10) and β-sheet amyloid species (32.4% of ThS labelling overlapping with that of 105A, and 77.2% of 105A labelling overlapping with that of ThS), and surrounded by α-helical species of mouse AChE-S (16.3% of HR2 labelling overlapping with that of 105A, and 67.4% of 105A labelling overlapping with that of HR2; 7.7% of KD69 labelling overlapping with that of 105A, and 51.4% of 105A labelling overlapping with that of KD69) (Fig. 12*B*). Both 3313 and 3314 antisera labelled mouse AChE-S in mature plaques containing an amyloid mass (ThS) and Aβ species (Bam10)(Fig. 13). Indeed, 69% and 31.4% of ThS labelling overlapped with that of 3313 and 3314 respectively, and 68.2% and 87.4% of 3313 and 3314 labelling respectively overlapped with that of ThS; also 55.8% and 81.8% of Bam10 labelling overlapped with that of 3313 and 3314 respectively, and 27% and 23.8% of 3313 and 3314 labelling respectively overlapped with that of Bam10. Moreover, 3313 and 3314 labelling colocalised but also surrounded that of mouse AChE-S β-sheet species (65.2% and 61% of 105A labelling overlapped with that of 3313 and 3314 respectively, and 4.9% and 8.2% of 3313 and 3314 labelling respectively overlapped with that of 105A).

Mature plaques in the cerebral cortex of hAChE-S/hAPPswe mice contained hAChE-S (KD69 and HR2) and Aβ species (Bam10)(Fig. 14*A*). The Aβ species showed some degree of colocalisation with hAChE-S (73.4% of Bam10 labelling overlapping with that of HR2, and 20.3% of HR2 labelling overlapping with that of Bam10; 65.4% of Bam10 labelling overlapping with that of KD69, and 35.8% of KD69 labelling overlapping with that of Bam10), and both hAChE-S (HR2 and KD69) and hAChE-S species with α-helical T40 (KD69) surrounded the Aβ species. This labelling pattern is reminiscent of that observed in AD with hAChE-S being associated with senile plaques (24). Importantly, hAChE-S β-sheet species (105A) were detected in mature plaques, representing only a proportion of the hAChE-S present (14.7% of HR2 labelling overlapping with that of 105A, and 73.1% of 105A labelling overlapping with that of HR2), and surrounded by α-helical forms (6.5% of KD69 labelling overlapping with that of 105A, and 40.2% of 105A labelling overlapping with that of KD69)(Fig. 14*B*). The plaque hAChE-S β-sheet staining partly co-localised with β-sheet amyloid species (12.1% of ThS labelling overlapping with that of 105A, and 47.9% of 105A labelling overlapping with that of ThS) and Aβ species (5.5% of Bam10 labelling overlapping with that of 105A, and 38.6% of 105A labelling overlapping with that of Bam10). In each case, the plaque hAChE-S β-sheet species tended to be centrally located within the mass of amyloids. 3313 and 3314 labelled hAChE-S species associated with fibrilar amyloids (38.7% and 42% of ThS labelling overlapped with that of 3313 and 3314 respectively, and 75% and 79.6% of 3313 and 3314 labelling respectively overlapped with that of ThS), Aβ species (49.1% and 86.2% of Bam10 labelling overlapped with that of 3313 and 3314 respectively, and 17.3% and 13.2% of 3313 and 3314 labelling respectively overlapped with that of Bam10) and β-sheets hAChE-S species (50.6% and 32.8% of 105A labelling overlapped with that of 3313 and 3314 respectively, and 10.1% and 6.7% of 3313 and 3314 labelling respectively overlapped with that of 105A)(Fig. 15). The patterns of colocalisation appeared whenever plaques were detected. The species detected by both 3313 and 3314 appeared to represent only a proportion of the fibrilar amyloids (compare, for example, ThS versus 3313 or 3314; see above), and to be centrally localised within the amyloid burden. In contrast, when compared with Aβ species (Bam10) or hAChE-S β-sheet species (105A), the hAChE-S species labelled with 3313 not only colocalised with the Aβ and hAChE-S β-sheet species but extended to the surrounding areas as if encapsulating these in their centre. Interestingly, the pattern with 3314 was different. Some colocalisation was observed with Aβ and hAChE-S β-sheet species, but 3314 also labelled hAChE-S species in discrete and distinct areas from these (Fig. 15*B*, *arrows*). Moreover, the labelling of both 3313 and 3314 overlapped to some degree with that of HR2 (globular part of AChE-S) and that of KD69 (α-helical T40)(Fig. S7). This suggests that 3313 and 3314 also recognise, to some level, AChE-S in an *in-vivo* context. These experiments provide the first *in-vivo* evidence of the conformation of hAChE-S related species located in senile mature plaques and colocalising with Aβ species and fibrilar amyloids.

DISCUSSION

We previously showed that IDE-dependent cleavage of hAChE-S non-amyloidogenic and α-helical oligomerisation domain, T40, generates new peptide species (28). As a mixture, they form β-sheets, are surface active, assemble into amyloid protofibrils and seed Aβ aggregation. In monomeric G1 AChE-S, T40 remains exposed and susceptible to proteolysis, even in bovine AChE-S tetramers (32). Despite clues pointing at T40, the exact nature of the hAChE-S domain involved remains uncertain (18-21). Thus, identifying IDE-derived amyloidogenic hAChE-S species should provide targets to characterise and identify brain fibrilogenic hAChE-S species.

Eleven hAChE-S peptides from IDE-dependent cleavage of T40 were assessed singly rather than mixtures, as amyloidogenic species. Two T40 regions had exceptionally strong β-sheet propensity, WKAEFHR and SYMVHWK. The two peptides with strongest propensity contained the latter region, $AChE_{590-598}$ (RWSSYMVHW) and $AChE_{594-598}$ (YMVHW). In terms of conformation, we identified negative effects of the T40 N-terminus. At the lowest concentration, after neutralisation, only $AChE_{590-598}$ (RWSSYMVHW) adopted a dominant β-sheet conformation. At higher concentration or in presence of SDS as a membrane mimicking agent, other peptides also adopted a β-sheet conformation (e.g. $AChE_{589-598}$, HRWSSYMVHW). These results imply that the *in-vivo* environment, in which these peptides are found (e.g. vicinity of cellular membranes), drastically influences their amyloidogenic behaviour. $AChE_{590-598}$ (RWSSYMVHW) was the most surface-active peptide, a property involved in amyloid toxicity. Only six peptides could fibrilise by themselves, most of them able to adopt a degree of β-sheet conformation and containing YMVH. Individually, $AChE_{585-597}$ (KAEFHRWSSYMVH) and $AChE_{590-598}$ (RWSSYMVHW), the best two fibrilising peptides, allowed fibrilisation of T40-IDE peptides that did not fibrilise alone. Importantly, most individual peptide seeds, except $AChE_{584-603}$, significantly reduced Aβ lag phase, with $AChE_{590-598}$ (RWSSYMVHW) among the most effective. We identified RWSSYMVHW ($AChE_{590-598}$) as the most amyloidogenic peptide and generated two new polyclonal antibodies against it, 3313 and 3314. These recognised peptides that fibrillise or adopt a β-sheet conformation, although recognition levels varied. They also had a different specificity to Mab 105A, except for recognising $AChE_{584-603}$ (WKAEFHRWSSYMVHWKNQFD). Having created and characterised specific new reagents against hAChE-S T40-derived species of diverse properties, we probed for hAChE-S derived peptides, or hAChE-S with a still attached but proteolytically digested T40 in brains of 12 month old controls, hAChE-S or hAPPswe single transgenic mice (Tg2576, APP_{695} isoform), and hAChE-S/hAPPswe double transgenic mice.

In hAChE-S mice, the transgene had been shown to provide greater AChE-S activity in cerebral cortex, doubling the total AChE-S activity but triggering no plaque formation (37). Therefore, it was unsurprising that only antibodies against globular hAChE-S (HR2) and T40 (KD69) achieved labelling.

By 8 to 9 months, hAPPswe mice began developing classic amyloid plaques in cerebral cortex, as we saw with ThS and anti-Aβ Bam10 in 12 month old mice (37,57). The plaques were also rich with HR2 and KD69 labelling. Aβ treatment of cultured mouse neuroblastoma and mouse primary neuronal cultures triggers elevated levels of mouse AChE-S expression and activity (58). Despite an overall decrease of hAChE-S activity in human AD patient brains, it rises in amyloid plaques and NFT at very early stages of amyloid deposition (15,59). Also, various hAPP transgenic mice showed selective elevation of mouse AChE activity in brain areas linked to severe AD pathology, in particular cores of amyloid plaques in the neocortex, as we saw with Mab 105A anti-AChE$_{586\text{-}599}$ (60-63). Some hAPP mice models also have higher levels of G1 monomeric mouse AChE-S (62). Moreover, in pathologically relevant cortical extracts of Tg2576 mice, Aβ deposition began as early as 4 months before overt pathology began, and the activity of abnormal glycosylated G1 forms of mouse AChE was rising (63,64). These Aβ-triggered elevations of mouse AChE-S, potentially proteolytically susceptible monomeric G1 forms, combined with high amino-acid homology in hAChE-S and its mouse equivalent, explain plaque labelling by HR2, KD69, 105A, 3313 and 3314 in the Tg2576 mice but only in the context of human Aβ plaque deposition. We saw no labelling in wild-type mice with mouse APP and AChE-S that never develop plaques (65). hAChE-S is also elevated in human brain tissue immediately adjacent to amyloid plaques (66). Therefore, local neurons reacting to increased levels of soluble Aβ, Aβ deposition, and amyloid burden in general, could drive AChE-S expression. In turn, proteolytic impact of highly expressed AChE-S could generate amyloidogenic β-sheet species and create a vicious circle of further Aβ seeding or deposition.

In hAPPswe and hAPPswe/hAChE mice, amyloid plaques were detected in brain areas relevant for AD. Indeed, in the cerebral cortex, the motor, orbital and prelimbic sub-areas all labelled with plaques, as observed in human AD. These cortical sub-areas are also amongst the most heavily affected by Aβ burden in another mouse model of AD (b6.Cg-Tg(APPswe/PSEN1De9)85Dbo/j, chimeric mouse/human APPswe and human presilin-1 gene lacking exon 9) (67). In the orbitofrontal cortex of ~16 month old Tg2576 transgenic mice, Aβ deposition was modest (68). Likewise, motor cortex in 12-month old double transgenic mice tested with all our antibodies/reagent, showed the heaviest amyloid burden, with fewer plaques in the orbital area (68). In the olfactory bulb and cortex of Tg2576 transgenic mice, non-fibrilar Aβ deposition and plaque appearance occur earlier than in any other brain areas (6 months), with deposition in the olfactory bulb as one of the earliest pathological changes (68-70). ThS stained mainly the olfactory bulb granule layer, and Aβ deposition occurred across other layers as the mice aged, correlating with progressive olfactory impairments, resembling those in human AD. In the olfactory cortex and bulb of our double transgenic mice, the observed plaque repartition (anterior olfactory nucleus, and granular layer of the bulb) was similar to that described in Tg2576 and b6.Cg-Tg mouse models (67). These areas had amongst the heaviest amyloid burden. Senile plaques and NFT are commonly found in human olfactory cortex and bulb, and also in brain regions receiving input from it (69,71). In human dementia, the anterior olfactory nucleus has reduced neuron density, shows NFTs, with number and densities paralleling dementia severity, and contains mature senile plaques when dementia is severe. Thus in our AD mouse model, amyloid species, Aβ and AChE-S species accumulate in plaques in various and distinct brain regions that parallel those in other AD mouse models and more importantly in human AD (72,73).

Mature plaques in the cerebral cortex of our double transgenic mice contained hAChE-S, hAChE-S species, β-sheet amyloid species, and Aβ. Both intact hAChE-S (HR2 and KD69) and hAChE-S species with α-helical T40 (KD69) surrounded the β-sheet amyloid (ThS) and Aβ (Bam10). In contrast, hAChE-S species (3313 and 3314) and hAChE-S species with a β-sheet conformation (105A) colocalised with β-sheet amyloid (ThS) and Aβ species (Bam10) at a more central location within the amyloid burden. In human AD brains, histochemistry for cholinesterase activity showed that both the central core of plaques and its surrounding rim stained strongly and consistently, which also labelled with ThS and Mab 4G8 anti-Aβ (59). hAChE activity was also found associated with mature amyloid plaques, both at the neuritic core and periphery, by electron microscopy of human AD brains (74). Our findings are in perfect agreement with previous reports.

Although linked to AD pathology, and in contrast to APP and Aβ, hAChE-S has been neglected in terms of understanding its role and physiology during AD. Prior research mostly focussed on inhibiting cholinesterase activity for short-term symptomatic relief. Clearly, the relationships among cholinergic dysfunction, cognitive deficit and pathological structures remain poorly understood. To our knowledge, our study is the first to investigate conformations adopted by hAChE-S within plaques and the presence of hAChE-S related species. Our experiments provide the first *in-vivo* evidence that many Aβ-containing amyloid plaques become associated with hAChE-S in α-helical conformation, and related species in β-sheet conformation. The β-sheet species may be the result of proteolytic cleavage generating either T40-derived isolated amyloidogenic peptides and/or shortened and amyloidogenic T40 not released from hAChE-S globular part. We also show that some individual species generated by proteolytic digestion of hAChE-S T40 domain adopt a β-sheet conformation, are surface active, highly amyloidogenic, and able to seed Aβ. This sets the stage for further studies on pathologically relevant Aβ-hAChE-S interactions (e.g. seeding) in hAChE/hAPPswe mice. Using double transgenic mice for such purposes has previously proven valid and successful (75). As in prion disease, the spread of AD pathology may be due to template-directed misfolding by progressive seeding of amyloid aggregation, which can spread into adjacent and interconnected neurons (76). This is supported by the following evidence: in mice that do not normally develop AD pathology, induced Aβ deposition occurs *de novo* in brain areas (e.g. cortex) far from the original hippocampal injection site of brain extracts from AD patients; induction of senile plaques in the brains of primates by intracerebral injection of human AD brain homogenates; and seeded Aβ aggregation in an APP transgenic mouse model by intracerebral infusion of AD brain extracts (77-79). In AD, amyloid propagation and dissemination to neighbouring neurons or brain areas is conceivable for Aβ as it is naturally present in the extracellular space and can diffuse widely without needing to cross membranes. In mammals, globular hAChE-S is mostly a G1 soluble monomer and a G4 tetrameric membrane-bound form (66,80). As AD progresses, there is selective reduction or loss of G4 tetramers and a rise in G1 monomers in cerebral cortex and cerebrospinal fluid (66,81,82). Furthermore, in cerebral cortex of severely affected AD patients with heavy Aβ loads, G4 hAChE-S activity falls ~50%, and G1 forms rise (66). Rising G1 activity also correlates positively with density of cortical amyloid deposits. In bovines, AChE T40 is vulnerable to proteolysis even in tetramers, and is naturally cleaved or truncated in foetal bovine serum G1 AChE (32,33). Hence, in AD, it is plausible that increased hAChE-S G1 forms that would be extracellular, soluble and with a proteolytically susceptible T40 could lead to the generation of hAChE-S derived amyloidogenic species able to seed Aβ aggregation. To date, therapies for diseases like AD do not modify the pathological process, but only offer temporary symptomatic alleviation. Template-directed misfolding by seeding of Aβ by hAChE-S, but also cellular dissemination of amyloidogenic species could offer novel therapeutic strategies, to delay propagation by stabilising native protein conformations.

EXPERIMENTAL PROCEDURES

Synthetic peptides, antibodies and mouse brains-Lyophilised T40-IDE derived peptides and synthetic human $A\beta_{1-40}$ (EZBiolab, Carmel, IN, USA) were purchased already purified by reverse-phase high performance liquid chromatography with a C18 column. Before use, the T40-IDE peptides were resuspended at 2mg/ml in water, and Aβ was resuspended in DMSO at 1.6 mM. Aβ was then sonicated and centrifuged for 1 hr at 15,000 g at + 4°C (to remove any pre-aggregated species). DMSO was used to maintain Aβ in a monomeric pool lacking any β-sheet secondary structures (83).

Specific mouse Mab 105A anti-$AChE_{586-599}$ in a β-sheet conformation and rabbit polyclonal KD69 anti-α helical T40 were previously described (30). Two rabbit polyclonal antibodies anti-$AChE_{590-598}$, named 3313 and 3314, were produced by Cambridge Research Biochemicals (Billingham, Cleveland, UK) using C-Ahx-$AChE_{590-598}$-acid coupled at the N-terminus to keyhole limpet hemocyanin (KLH) as an antigen, via standard immunisation procedures. Other antibodies used were mouse Mab HR2 anti-cerebellar hAChE-S, and Mab Bam10 anti-Aβ (first 12 residues). Brains from 12 month-old wild-type control, hAChE-S single transgenic, hAPPswe single transgenic (Tg2576, APP_{695} isoform), and hAChE-S/hAPPswe double transgenic mice from the Brimijoin lab (18).

Circular dichroism (CD)-Far UV spectra (250 to 190 nm) before and after pH neutralisation (50 mM NaH_2PO_4, pH 7.2 final) of 100 or 200 μM T40-IDE peptides in absence or presence of 10 mM SDS. The mean spectra of multiple scans (speed, 50 nm min^{-1}, response time 4 sec) were collected at 20°C in a quartz cuvette (1 mm path length) using a Jasco J-720 spectropolarimeter. The spectra were blank subtracted and normalised to molar ellipticity. At least three independent assays were performed. Statistical analysis was by two-sample t-test. To determine the percentage of secondary structures, the CD spectra were analysed with CONTINLL from the CDPro package (84).

Fibrilisation experiments-100 or 200 μM T40-IDE peptides were incubated with 165 μM ThT in PBS in a 100 μl reaction volume. Thioflavin T (ThT) fluorescence (excitation 450 nm, emission 480 nm) was measured daily in 96-well plates (black wall, clear bottom, Greiner Bio-One, Stonehouse, Gloucestershire, UK), at 37°C every 6.7 min with 5 min orbital shaking after every measurement, on a BMG Polarstar plate reader (BMG labtech, Aylesbury, Buckinghamshire, UK) using a bottom-bottom configuration (optical fiber system detecting emission signal from the bottom of the well). Values in control wells (ThT/buffer) were subtracted from those of test wells (ThT/peptide). Kinetic parameters were calculated as follows: elongation rate was calculated from slope at the sigmoidal curve inflection point; plateau height was calculated by averaging the highest curve values (minimum of five); and the lag phase was calculated from the intercept on the time axis of the line tangent to the inflection point. Three or more independent assays were performed and analysed each with two-sample t-tests.

Co-fibrilisation-50 μM T40-IDE peptides were incubated with 50 μM AChE$_{590\text{-}598}$ or AChE$_{585\text{-}597}$, or 15 μM Aβ was incubated with 15 μM T40-IDE peptides, and the fibrilisation experiments were carried as described above.

Heterologous seeding-200 μM T40-IDE peptides in PBS were fibrilised for 2 hrs at room temperature with continuous shaking to generate seeds, and 15 μM Aβ$_{1\text{-}40}$ (DMSO stock) was incubated with 165 μM ThT in PBS (100 μl reaction volume), with or without 2 μM T40-IDE peptide seeds. ThT fluorescence was measured as described in *Fibrilisation experiments,* but readings were taken every 21 min, with 5 min shaking after each read. Control wells contained ThT, buffers and 2 μM seeds when required. Values in control wells (ThT/buffer with or without seeds) were subtracted from those in test wells (Aβ with or without seeds), assuring that seeds did not affect ThT fluorescence.

Transmission electron microscopy-100 μM T40-IDE peptides were harvested when the plateau phase was reached (as measured by ThT fluorescence emission). The solutions were adsorbed onto Formvar-coated 400 mesh copper grids, air dried, washed with distilled water, negatively stained with 2% aqueous uranyl acetate and viewed with a Tecnai electron microscope (Philips).

Surface activity measurement-Analyses were performed as previously described (47). Stock solutions of T40-IDE peptides were diluted to 50 μM in 200 mM sodium acetate pH 2 (100 μL final volume), and dispensed in a 96-well plate (black wall, clear bottom; Greiner Bio-One). Surface activity was measured at 37ºC, before and after neutralisation with 20 μL 1M NaH_2PO_4 pH7.2, at 450 nm on a BMG Polarstar plate reader at the central and offset positions. $\Delta OD = (OD_{offset} - OD_{central,\ neutral\ pH\ 2min} - (OD_{offset} - OD_{central})_{neutral\ pH}$. Three or more independent assays were performed and analysed by two-sample t-test.

Immuno-blot- To generate seeds, T40-IDE peptides were fibrilised (see above). Aβ fibrils were generated by incubating 199 μM Aβ in PBS and leaving it for one week at 37°C under shaking conditions. 2 μg T40-IDE peptide or peptide seeds, T40, Aβ, Aβ fibrils and 1 μg hAChE-S were blotted onto nitrocellulose membrane. This was blocked with 0.4% fish skin gelatin in PBS/0.5% tween 20, and incubated with rabbit polyclonal antibody 3313 or 3314, or mouse Mab 105A, followed by anti-rabbit or anti-mouse IgG conjugated to HRP. Products were visualized by enhanced chemiluminescence.

Immunolabelling and confocal microscopy- Deep-frozen mouse brain material from control, single and double transgenic mice was derived at the Mayo Clinic (Mayo Clinic study conducted under approval of IACUC study protocol A67914-15-R18).

Mouse brains embedded in Optimal cutting temperature compound generated 12 μm coronal sections kept frozen at -20ºC until used. Sections were fixed in 4% paraformaldehyde on ice for 30 min and permeabilised with 0.4% Triton X-100 for 30 min at room temperature. ABC mouse-on-mouse (M.O.M.) or Vectastain Elite ABC rabbit IgG kits were used, following manufacturer instructions (Vector laboratories, Burlingame, CA, USA). To block non-specific binding of components, avidin and biotin (Vector kit) were applied consecutively for 15 min at room temp. With mouse primary antibody, endogenous mouse Ig sections were treated with Vector M.O.M. mouse IgG blocking reagent for one hour at room temperature before protein blocking with M.O.M. diluent for 5 min at room temperature. With rabbit primary antibodies, sections were treated with Vectastain blocking serum, and labelled with one antibody or two. Single-labelled sections were incubated with primary antibody (30 min), M.O.M. anti-mouse or Vectastain anti-rabbit biotinylated antisera (10 min), followed by avidin-conjugated to peroxidase (5 min) and DAB as chromagen (2 min, Vector Labs), or avidin- FITC conjugate, or Texas red (5 min). Double-labelled sections were incubated with first antibody as above. Then, to prevent interactions between first and second labelling sets, Vector avidin and biotin were applied consecutively for 15 min at room temperature. Then, sections were treated 1 hr with M.O.M. mouse IgG blocking diluent or Vectastain normal blocking serum, incubated with a second primary antibody (30 min), M.O.M. anti-mouse or Vectastain anti-rabbit biotinylated antisera (10 min) and avidin conjugated to FITC or to Texas red (5 min). Finally section nuclei were counterstained with Harris haematoxylin (10 sec) before mounting in mowiol (+4ºC overnight). When required, sections were stained with 1% Thioflavin S (ThS) in water for 5 min at room temperature before mounting. All imaging used a LSM 510 META microscope (Carl Zeiss, Inc.) on an Axio Imager Z1 with a 40 × 0.75 objective or a 63 × 1.4 oil immersion lens. Laser lines were 488 nm and 543 nm to excite FITC and Texas Red respectively. Fluorescence was measured with the following filters: 505 – 530 nm band pass for FITC, 625 – 743 nm band pass for Texas Red. Z-stacks were collected with 16 μm interval between slices. Tiling functions of the confocal microscope collected a series of images spanning the whole brain section. Images were analysed with Image Browser software (Carl Zeiss, Inc.).

Colocalisation (fluorescence overlap) was measured using the FIJI plugin JACoP (85). Labelling area and intensity were measured in FIJI using a Huang threshold, ROI manager and a set measurement analysis.

Acknowledgements: L.J. was supported by a research grant from Synaptica Ltd. We would like to thank Richard Stillion (Sir William Dunn School of Pathology, University of Oxford) for his assistance and help with the preparation and sectioning of the mouse brains. We are also grateful to Howard Womersley for epitope mapping of the 105A monoclonal by phage display.

Conflict of interest: The authors declare that they have no conflicts of interest with the contents of this article.

Author contributions: LJ and DJV designed the study. LJ performed the experiments. LJ performed the analysis and LJ led the writing of the paper. SB provided the brains of control and transgenic mice. LJ, SB and DJV discussed results, interpreted the data and helped in polishing the manuscript.

REFERENCES

1. Stefani, M., and Dobson, C. M. (2003) Protein aggregation and aggregate toxicity: new insights into protein folding, misfolding diseases and biological evolution. *J Mol Med (Berl)* **81**, 678-699
2. Chiti, F., and Dobson, C. M. (2006) Protein misfolding, functional amyloid, and human disease. *Annu Rev Biochem* **75**, 333-366
3. Harper, J. D., and Lansbury, P. T., Jr. (1997) Models of amyloid seeding in Alzheimer's disease and scrapie: mechanistic truths and physiological consequences of the time-dependent solubility of amyloid proteins. *Annu. Rev. Biochem.* **66**, 385-407
4. Klimov, D. K., and Thirumalai, D. (2003) Dissecting the assembly of Abeta16-22 amyloid peptides into antiparallel beta sheets. *Structure* **11**, 295-307

5. West, M. W., Wang, W., Patterson, J., Mancias, J. D., Beasley, J. R., and Hecht, M. H. (1999) De novo amyloid proteins from designed combinatorial libraries. *Proc Natl Acad Sci U S A* **96**, 11211-11216
6. Zanuy, D., Haspel, N., Tsai, H. H., Ma, B., Gunasekaran, K., Wolfson, H. J., and Nussinov, R. (2004) Side chain interactions determine the amyloid organization: a single layer beta-sheet molecular structure of the calcitonin peptide segment 15-19. *Phys Biol* **1**, 89-99
7. Smith, C. K., and Regan, L. (1995) Guidelines for protein design: the energetics of beta sheet side chain interactions. *Science* **270**, 980-982
8. Haass, C., and Selkoe, D. J. (2007) Soluble protein oligomers in neurodegeneration: lessons from the Alzheimer's amyloid beta-peptide. *Nat Rev Mol Cell Biol* **8**, 101-112
9. Kolisnyk, B., Al-Onaizi, M., Soreq, L., Barbash, S., Bekenstein, U., Haberman, N., Hanin, G., Kish, M. T., Souza da Silva, J., Fahnestock, M., Ule, J., Soreq, H., Prado, V. F., and Prado, M. A. M. (2017) Cholinergic Surveillance over Hippocampal RNA Metabolism and Alzheimer's-Like Pathology. *Cereb Cortex* **27**, 3553-3567
10. Shaked, I., Meerson, A., Wolf, Y., Avni, R., Greenberg, D., Gilboa-Geffen, A., and Soreq, H. (2009) MicroRNA-132 potentiates cholinergic anti-inflammatory signaling by targeting acetylcholinesterase. *Immunity* **31**, 965-973
11. Francis, P. T., Palmer, A. M., Snape, M., and Wilcock, G. K. (1999) The cholinergic hypothesis of Alzheimer's disease: a review of progress. *J Neurol Neurosurg Psychiatry* **66**, 137-147
12. Madhusudan, A., Sidler, C., and Knuesel, I. (2009) Accumulation of reelin-positive plaques is accompanied by a decline in basal forebrain projection neurons during normal aging. *Eur J Neurosci* **30**, 1064-1076
13. Auld, D. S., Kornecook, T. J., Bastianetto, S., and Quirion, R. (2002) Alzheimer's disease and the basal forebrain cholinergic system: relations to beta-amyloid peptides, cognition, and treatment strategies. *Prog Neurobiol* **68**, 209-245
14. Coyle, J. T., Price, D. L., and Delong, M. R. (1983) Alzheimers-Disease - a Disorder of Cortical Cholinergic Innervation. *Science* **219**, 1184-1190
15. Ulrich, J., Meierruge, W., Probst, A., Meier, E., and Ipsen, S. (1990) Senile Plaques - Staining for Acetylcholinesterase and A4-Protein - a Comparative-Study in the Hippocampus and Entorhinal Cortex. *Acta Neuropathol* **80**, 624-628
16. Dubois, B., Chupin, M., Hampel, H., Lista, S., Cavedo, E., Croisile, B., Louis Tisserand, G., Touchon, J., Bonafe, A., Ousset, P. J., Ait Ameur, A., Rouaud, O., Ricolfi, F., Vighetto, A., Pasquier, F., Delmaire, C., Ceccaldi, M., Girard, N., Dufouil, C., Lehericy, S., Tonelli, I., Duveau, F., Colliot, O., Garnero, L., Sarazin, M., Dormont, D., Hippocampus Study, G., and Hippocampus Study, G. (2015) Donepezil decreases annual rate of hippocampal atrophy in suspected prodromal Alzheimer's disease. *Alzheimers Dement* **11**, 1041-1049
17. Pavlov, V. A., Parrish, W. R., Rosas-Ballina, M., Ochani, M., Puerta, M., Ochani, K., Chavan, S., Al-Abed, Y., and Tracey, K. J. (2009) Brain acetylcholinesterase activity controls systemic cytokine levels through the cholinergic anti-inflammatory pathway. *Brain Behav Immun* **23**, 41-45
18. Rees, T. M., Berson, A., Sklan, E. H., Younkin, L., Younkin, S., Brimijoin, S., and Soreq, H. (2005) Memory deficits correlating with acetylcholinesterase splice shift and amyloid burden in doubly transgenic mice. *Curr Alzheimer Res* **2**, 291-300
19. Alvarez, A., Alarcon, R., Opazo, C., Campos, E. O., Munoz, F. J., Calderon, F. H., Dajas, F., Gentry, M. K., Doctor, B. P., De Mello, F. G., and Inestrosa, N. C. (1998) Stable complexes involving acetylcholinesterase and amyloid-beta peptide change the biochemical properties of the enzyme and increase the neurotoxicity of Alzheimer's fibrils. *J Neurosci* **18**, 3213-3223
20. Inestrosa, N. C., Alvarez, A., Perez, C. A., Moreno, R. D., Vicente, M., Linker, C., Casanueva, O. I., Soto, C., and Garrido, J. (1996) Acetylcholinesterase accelerates assembly of amyloid-beta-peptides into Alzheimer's fibrils: possible role of the peripheral site of the enzyme. *Neuron* **16**, 881-891
21. Berson, A., Knobloch, M., Hanan, M., Diamant, S., Sharoni, M., Schuppli, D., Geyer, B. C., Ravid, R., Mor, T. S., Nitsch, R. M., and Soreq, H. (2008) Changes in readthrough acetylcholinesterase expression modulate amyloid-beta pathology. *Brain* **131**, 109-119

22. Alvarez, A., Opazo, C., Alarcon, R., Garrido, J., and Inestrosa, N. C. (1997) Acetylcholinesterase promotes the aggregation of amyloid-beta-peptide fragments by forming a complex with the growing fibrils. *J Mol Biol* **272**, 348-361

23. Saez-Valero, J., Sberna, G., McLean, C. A., and Small, D. H. (1999) Molecular isoform distribution and glycosylation of acetylcholinesterase are altered in brain and cerebrospinal fluid of patients with Alzheimer's disease. *J Neurochem* **72**, 1600-1608

24. Wright, C. I., Geula, C., and Mesulam, M. M. (1993) Neurological cholinesterases in the normal brain and in Alzheimer's disease: relationship to plaques, tangles, and patterns of selective vulnerability. *Ann Neurol* **34**, 373-384

25. Geula, C., and Mesulam, M. (1989) Special properties of cholinesterases in the cerebral cortex of Alzheimer's disease. *Brain Res* **498**, 185-189

26. Berson, A., and Soreq, H. (2010) It all starts at the ends: multifaceted involvement of C- and N-terminally modified cholinesterases in Alzheimer's disease. *Rambam Maimonides Med J* **1**, e0014

27. Farchi, N., Ofek, K., Podoly, E., Dong, H., Xiang, Y. Y., Diamant, S., Livnah, O., Li, J., Hochner, B., Lu, W. Y., and Soreq, H. (2007) Peripheral site acetylcholinesterase blockade induces RACK1-associated neuronal remodeling. *Neurodegener Dis* **4**, 171-184

28. Jean, L., Thomas, B., Tahiri-Alaoui, A., Shaw, M., and Vaux, D. J. (2007) Heterologous amyloid seeding: revisiting the role of acetylcholinesterase in Alzheimer's disease. *PLoS One* **2**, e652

29. Diamant, S., Podoly, E., Friedler, A., Ligumsky, H., Livnah, O., and Soreq, H. (2006) Butyrylcholinesterase attenuates amyloid fibril formation in vitro. *Proc Natl Acad Sci U S A* **103**, 8628-8633

30. Cottingham, M. G., Voskuil, J. L., and Vaux, D. J. (2003) The intact human acetylcholinesterase C-terminal oligomerization domain is alpha-helical in situ and in isolation, but a shorter fragment forms beta-sheet-rich amyloid fibrils and protofibrillar oligomers. *Biochemistry* **42**, 10863-10873

31. Yoon, S., and Welsh, W. J. (2004) Detecting hidden sequence propensity for amyloid fibril formation. *Protein Sci* **13**, 2149-2160

32. Liao, J., Boschetti, N., Mortensen, V., Jensen, S. P., Koch, C., Norgaard-Pedersen, B., and Brodbeck, U. (1994) Characterization of salt-soluble forms of acetylcholinesterase from bovine brain. *J Neurochem* **63**, 1446-1453

33. Saxena, A., Hur, R. S., Luo, C., and Doctor, B. P. (2003) Natural monomeric form of fetal bovine serum acetylcholinesterase lacks the C-terminal tetramerization domain. *Biochemistry* **42**, 15292-15299

34. Prusiner, S. B. (1996) Molecular biology and pathogenesis of prion diseases. *Trends Biochem Sci* **21**, 482-487

35. Meyer-Luehmann, M., Coomaraswamy, J., Bolmont, T., Kaeser, S., Schaefer, C., Kilger, E., Neuenschwander, A., Abramowski, D., Frey, P., Jaton, A. L., Vigouret, J. M., Paganetti, P., Walsh, D. M., Mathews, P. M., Ghiso, J., Staufenbiel, M., Walker, L. C., and Jucker, M. (2006) Exogenous induction of cerebral beta-amyloidogenesis is governed by agent and host. *Science* **313**, 1781-1784

36. Padrick, S. B., and Miranker, A. D. (2002) Islet amyloid: phase partitioning and secondary nucleation are central to the mechanism of fibrillogenesis. *Biochemistry* **41**, 4694-4703

37. Rees, T., Hammond, P. I., Soreq, H., Younkin, S., and Brimijoin, S. (2003) Acetylcholinesterase promotes beta-amyloid plaques in cerebral cortex. *Neurobiol Aging* **24**, 777-787

38. Beeri, R., Andres, C., Lev-Lehman, E., Timberg, R., Huberman, T., Shani, M., and Soreq, H. (1995) Transgenic expression of human acetylcholinesterase induces progressive cognitive deterioration in mice. *Curr Biol* **5**, 1063-1071

39. Beeri, R., Le Novere, N., Mervis, R., Huberman, T., Grauer, E., Changeux, J. P., and Soreq, H. (1997) Enhanced hemicholinium binding and attenuated dendrite branching in cognitively impaired acetylcholinesterase-transgenic mice. *J Neurochem* **69**, 2441-2451

40. Sternfeld, M., Shoham, S., Klein, O., Flores-Flores, C., Evron, T., Idelson, G. H., Kitsberg, D., Patrick, J. W., and Soreq, H. (2000) Excess "read-through" acetylcholinesterase attenuates but

the "synaptic" variant intensifies neurodeterioration correlates. *Proc Natl Acad Sci U S A* **97**, 8647-8652

41. Sormanni, P., Aprile, F. A., and Vendruscolo, M. (2015) The CamSol method of rational design of protein mutants with enhanced solubility. *J Mol Biol* **427**, 478-490
42. Fernandez-Escamilla, A. M., Rousseau, F., Schymkowitz, J., and Serrano, L. (2004) Prediction of sequence-dependent and mutational effects on the aggregation of peptides and proteins. *Nat Biotechnol* **22**, 1302-1306
43. Maurer-Stroh, S., Debulpaep, M., Kuemmerer, N., Lopez de la Paz, M., Martins, I. C., Reumers, J., Morris, K. L., Copland, A., Serpell, L., Serrano, L., Schymkowitz, J. W., and Rousseau, F. (2010) Exploring the sequence determinants of amyloid structure using position-specific scoring matrices. *Nat Methods* **7**, 237-242
44. LeVine, H., 3rd. (1993) Thioflavine T interaction with synthetic Alzheimer's disease beta-amyloid peptides: detection of amyloid aggregation in solution. *Protein Sci* **2**, 404-410
45. Lopes, D. H., Meister, A., Gohlke, A., Hauser, A., Blume, A., and Winter, R. (2007) Mechanism of islet amyloid polypeptide fibrillation at lipid interfaces studied by infrared reflection absorption spectroscopy. *Biophys J* **93**, 3132-3141
46. Soreghan, B., Kosmoski, J., and Glabe, C. (1994) Surfactant properties of Alzheimer's A beta peptides and the mechanism of amyloid aggregation. *J Biol Chem* **269**, 28551-28554
47. Cottingham, M. G., Bain, C. D., and Vaux, D. J. (2004) Rapid method for measurement of surface tension in multiwell plates. *Lab Invest* **84**, 523-529
48. Chi, E. Y., Frey, S. L., Winans, A., Lam, K. L., Kjaer, K., Majewski, J., and Lee, K. Y. (2010) Amyloid-beta fibrillogenesis seeded by interface-induced peptide misfolding and self-assembly. *Biophys J* **98**, 2299-2308
49. Jean, L., Lee, C. F., Lee, C., Shaw, M., and Vaux, D. J. (2010) Competing discrete interfacial effects are critical for amyloidogenesis. *FASEB J* **24**, 309-317
50. Jiang, D., Dinh, K. L., Ruthenburg, T. C., Zhang, Y., Su, L., Land, D. P., and Zhou, F. (2009) A kinetic model for beta-amyloid adsorption at the air/solution interface and its implication to the beta-amyloid aggregation process. *J Phys Chem B* **113**, 3160-3168
51. Morris, V. K., Ren, Q., Macindoe, I., Kwan, A. H., Byrne, N., and Sunde, M. (2011) Recruitment of class I hydrophobins to the air:water interface initiates a multi-step process of functional amyloid formation. *J Biol Chem* **286**, 15955-15963
52. Morinaga, A., Hasegawa, K., Nomura, R., Ookoshi, T., Ozawa, D., Goto, Y., Yamada, M., and Naiki, H. (2010) Critical role of interfaces and agitation on the nucleation of Abeta amyloid fibrils at low concentrations of Abeta monomers. *Biochim Biophys Acta* **1804**, 986-995
53. Jean, L., Lee, C. F., and Vaux, D. J. (2012) Enrichment of amyloidogenesis at an air-water interface. *Biophys J* **102**, 1154-1162
54. Wang, J., Dickson, D. W., Trojanowski, J. Q., and Lee, V. M. (1999) The levels of soluble versus insoluble brain Abeta distinguish Alzheimer's disease from normal and pathologic aging. *Exp Neurol* **158**, 328-337
55. Esparza, T. J., Wildburger, N. C., Jiang, H., Gangolli, M., Cairns, N. J., Bateman, R. J., and Brody, D. L. (2016) Soluble Amyloid-beta Aggregates from Human Alzheimer's Disease Brains. *Sci Rep* **6**, 38187
56. Collins-Praino, L. E., Francis, Y. I., Griffith, E. Y., Wiegman, A. F., Urbach, J., Lawton, A., Honig, L. S., Cortes, E., Vonsattel, J. P., Canoll, P. D., Goldman, J. E., and Brickman, A. M. (2014) Soluble amyloid beta levels are elevated in the white matter of Alzheimer's patients, independent of cortical plaque severity. *Acta Neuropathol Commun* **2**, 83
57. Hsiao, K., Chapman, P., Nilsen, S., Eckman, C., Harigaya, Y., Younkin, S., Yang, F., and Cole, G. (1996) Correlative memory deficits, Abeta elevation, and amyloid plaques in transgenic mice. *Science* **274**, 99-102
58. Hu, W., Gray, N. W., and Brimijoin, S. (2003) Amyloid-beta increases acetylcholinesterase expression in neuroblastoma cells by reducing enzyme degradation. *J Neurochem* **86**, 470-478
59. Moran, M. A., Mufson, E. J., and Gomez-Ramos, P. (1993) Colocalization of cholinesterases with beta amyloid protein in aged and Alzheimer's brains. *Acta Neuropathol* **85**, 362-369

60. Bronfman, F. C., Moechars, D., and Van Leuven, F. (2000) Acetylcholinesterase-positive fiber deafferentation and cell shrinkage in the septohippocampal pathway of aged amyloid precursor protein london mutant transgenic mice. *Neurobiol Dis* **7**, 152-168
61. Dumont, M., Lalonde, R., Ghersi-Egea, J. F., Fukuchi, K., and Strazielle, C. (2006) Regional acetylcholinesterase activity and its correlation with behavioral performances in 15-month old transgenic mice expressing the human C99 fragment of APP. *J Neural Transm (Vienna)* **113**, 1225-1241
62. Sberna, G., Saez-Valero, J., Li, Q. X., Czech, C., Beyreuther, K., Masters, C. L., McLean, C. A., and Small, D. H. (1998) Acetylcholinesterase is increased in the brains of transgenic mice expressing the C-terminal fragment (CT100) of the beta-amyloid protein precursor of Alzheimer's disease. *J Neurochem* **71**, 723-731
63. Apelt, J., Kumar, A., and Schliebs, R. (2002) Impairment of cholinergic neurotransmission in adult and aged transgenic Tg2576 mouse brain expressing the Swedish mutation of human beta-amyloid precursor protein. *Brain Res* **953**, 17-30
64. Fodero, L. R., Saez-Valero, J., McLean, C. A., Martins, R. N., Beyreuther, K., Masters, C. L., Robertson, T. A., and Small, D. H. (2002) Altered glycosylation of acetylcholinesterase in APP (SW) Tg2576 transgenic mice occurs prior to amyloid plaque deposition. *J Neurochem* **81**, 441-448
65. Saez-Valero, J., Fodero, L. R., White, A. R., Barrow, C. J., and Small, D. H. (2003) Acetylcholinesterase is increased in mouse neuronal and astrocyte cultures after treatment with beta-amyloid peptides. *Brain Res* **965**, 283-286
66. Arendt, T., Bruckner, M. K., Lange, M., and Bigl, V. (1992) Changes in acetylcholinesterase and butyrylcholinesterase in Alzheimer's disease resemble embryonic development--a study of molecular forms. *Neurochem Int* **21**, 381-396
67. Darvesh, S., Cash, M. K., Reid, G. A., Martin, E., Mitnitski, A., and Geula, C. (2012) Butyrylcholinesterase is associated with beta-amyloid plaques in the transgenic APPSWE/PSEN1dE9 mouse model of Alzheimer disease. *J Neuropathol Exp Neurol* **71**, 2-14
68. Wesson, D. W., Levy, E., Nixon, R. A., and Wilson, D. A. (2010) Olfactory dysfunction correlates with amyloid-beta burden in an Alzheimer's disease mouse model. *J Neurosci* **30**, 505-514
69. Franks, K. H., Chuah, M. I., King, A. E., and Vickers, J. C. (2015) Connectivity of Pathology: The Olfactory System as a Model for Network-Driven Mechanisms of Alzheimer's Disease Pathogenesis. *Front Aging Neurosci* **7**, 234
70. Lewis, J., Dickson, D. W., Lin, W. L., Chisholm, L., Corral, A., Jones, G., Yen, S. H., Sahara, N., Skipper, L., Yager, D., Eckman, C., Hardy, J., Hutton, M., and McGowan, E. (2001) Enhanced neurofibrillary degeneration in transgenic mice expressing mutant tau and APP. *Science* **293**, 1487-1491
71. Kovacs, T. (2004) Mechanisms of olfactory dysfunction in aging and neurodegenerative disorders. *Ageing Res Rev* **3**, 215-232
72. Christen-Zaech, S., Kraftsik, R., Pillevuit, O., Kiraly, M., Martins, R., Khalili, K., and Miklossy, J. (2003) Early olfactory involvement in Alzheimer's disease. *Can J Neurol Sci* **30**, 20-25
73. Price, J. L., Davis, P. B., Morris, J. C., and White, D. L. (1991) The distribution of tangles, plaques and related immunohistochemical markers in healthy aging and Alzheimer's disease. *Neurobiol Aging* **12**, 295-312
74. Carson, K. A., Geula, C., and Mesulam, M. M. (1991) Electron microscopic localization of cholinesterase activity in Alzheimer brain tissue. *Brain Res* **540**, 204-208
75. Holtzman, D. M., Bales, K. R., Tenkova, T., Fagan, A. M., Parsadanian, M., Sartorius, L. J., Mackey, B., Olney, J., McKeel, D., Wozniak, D., and Paul, S. M. (2000) Apolipoprotein E isoform-dependent amyloid deposition and neuritic degeneration in a mouse model of Alzheimer's disease. *Proc Natl Acad Sci U S A* **97**, 2892-2897
76. Brettschneider, J., Del Tredici, K., Lee, V. M., and Trojanowski, J. Q. (2015) Spreading of pathology in neurodegenerative diseases: a focus on human studies. *Nat Rev Neurosci* **16**, 109-120

77. Morales, R., Duran-Aniotz, C., Castilla, J., Estrada, L. D., and Soto, C. (2012) De novo induction of amyloid-beta deposition in vivo. *Mol Psychiatry* **17**, 1347-1353
78. Kane, M. D., Lipinski, W. J., Callahan, M. J., Bian, F., Durham, R. A., Schwarz, R. D., Roher, A. E., and Walker, L. C. (2000) Evidence for seeding of beta -amyloid by intracerebral infusion of Alzheimer brain extracts in beta -amyloid precursor protein-transgenic mice. *J Neurosci* **20**, 3606-3611
79. Baker, H. F., Ridley, R. M., Duchen, L. W., Crow, T. J., and Bruton, C. J. (1993) Evidence for the experimental transmission of cerebral beta-amyloidosis to primates. *Int J Exp Pathol* **74**, 441-454
80. Fishman, E. B., Siek, G. C., MacCallum, R. D., Bird, E. D., Volicer, L., and Marquis, J. K. (1986) Distribution of the molecular forms of acetylcholinesterase in human brain: alterations in dementia of the Alzheimer type. *Ann Neurol* **19**, 246-252
81. Atack, J. R., Perry, E. K., Bonham, J. R., Perry, R. H., Tomlinson, B. E., Blessed, G., and Fairbairn, A. (1983) Molecular forms of acetylcholinesterase in senile dementia of Alzheimer type: selective loss of the intermediate (10S) form. *Neurosci Lett* **40**, 199-204
82. Schegg, K. M., Harrington, L. S., Neilsen, S., Zweig, R. M., and Peacock, J. H. (1992) Soluble and membrane-bound forms of brain acetylcholinesterase in Alzheimer's disease. *Neurobiol Aging* **13**, 697-704
83. Shen, C. L., and Murphy, R. M. (1995) Solvent effects on self-assembly of beta-amyloid peptide. *Biophys J* **69**, 640-651
84. Sreerama, N., and Woody, R. W. (2000) Estimation of protein secondary structure from circular dichroism spectra: comparison of CONTIN, SELCON, and CDSSTR methods with an expanded reference set. *Anal Biochem* **287**, 252-260
85. Bolte, S., and Cordelieres, F. P. (2006) A guided tour into subcellular colocalization analysis in light microscopy. *J Microsc* **224**, 213-232

FOOTNOTES

The abbreviations used are: AChE, acetylchinesterase; AD, Alzheimer's disease; Aβ, amyloid-β peptide; APP, amyloid precursor protein; a.u., arbitrary units; BuChE, butyrylcholinesterase; CD, circular dichroism; DMSO, dimethyl sulfoxide; hAChE-S, synaptic form of the human acetylcholinesterase; HHI, hydrophobic-hydrophilic interface; HRP, horse raddish peroxidase; IDE, insulin degrading enzyme; KLH, keyhole limpet hemocyanin; Mab, monoclonal antibody; PBS, phosphate buffer saline; SDS, sodium dodecyl sulphate; ThS, thioflavin S; ThT, thioflavin T.

FIGURE LEGENDS

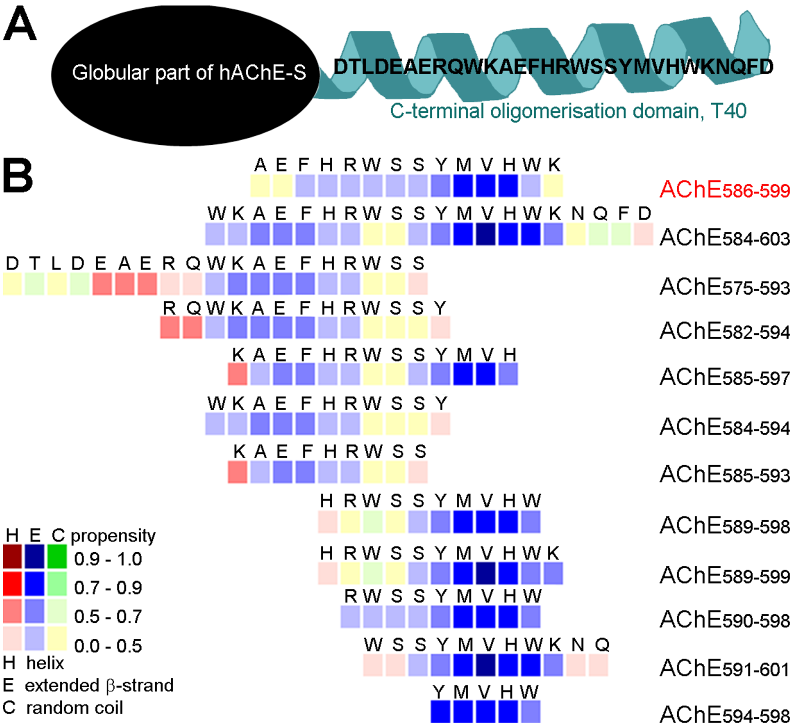

FIGURE 1. hAChE-S T40 and propensity of the T40-IDE synthetic peptides for conversion to non-native (hidden) β-strand. (*A*) Schematic of monomeric hAChE-S showing the exposed C-terminal oligomerisation domain, T40, in its native α-helical conformation. (*B*) The method developed by Yoon and Welsh was used (31). Propensities are presented numerically with low values indicating zero to low propensity and high values indicating high propensity to near certainty. Propensity for helices (*red squares*), β-strands (*blue squares*) and random coil (*green squares*). Hydrophobic residues are shown in green and aromatic residues in bold with a bigger font size. We have used AChE$_{586\text{-}599}$ as a benchmark, which is shown in red font.

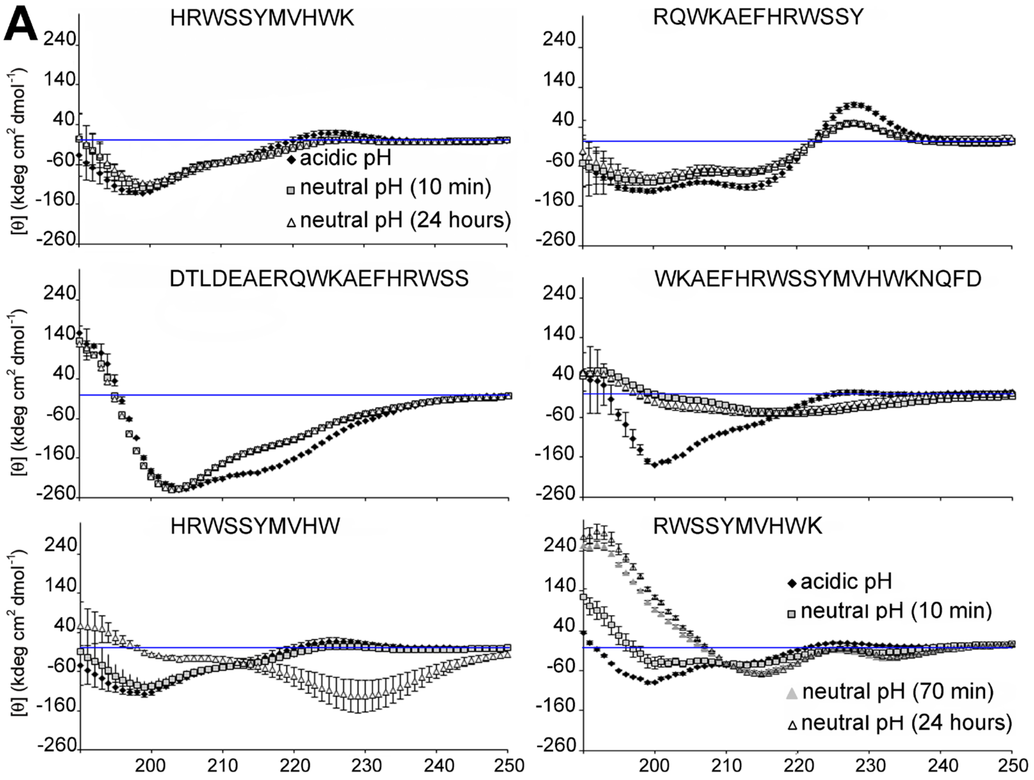

B

		Acidic pH	Neutral pH (10 min)	Neutral pH (24 hours)
AEFHRWSSYMVHWK	(AChE$_{586-599}$)	Random coil	Random coil	**β-sheet**
WKAEFHRWSSYMVHWKNQFD	(AChE$_{584-603}$)	β-sheet+β-turn+Rand. coil	**β-sheet**	α-helix+β-sheet+**R. coil**
DTLDEAERQWKAEFHRWSS	(AChE$_{575-593}$)	α-**helix**+Random coil	α-**helix**+Random coil	α-**helix**+Random coil
RQWKAEFHRWSSY	(AChE$_{582-594}$)	β-**sheet** + β-turn	β-**sheet** + β-turn	β-**sheet** + β-turn
KAEFHRWSSYMVH	(AChE$_{585-597}$)	**β-sheet** + Random coil	**β-sheet** + Random coil	**β-sheet** + Random coil
WKAEFHRWSSY	(AChE$_{584-594}$)	**β-sheet** + Random coil	**β-sheet** + Random coil	**β-sheet** + Random coil
KAEFHRWSS	(AChE$_{585-593}$)	**β-sheet** + Random coil	**β-sheet** + Random coil	**β-sheet** + Random coil
HRWSSYMVHW	(AChE$_{589-598}$)	β-sheet+β-turn+**R. coil**	β-sheet+β-turn+**R. coil**	α-**helix** + β-turn
HRWSSYMVHWK	(AChE$_{589-599}$)	β-sheet+β-turn+**R. coil**	β-sheet+β-turn+**R. coil**	β-sheet+β-turn+**R. coil**
RWSSYMVHW	(AChE$_{590-598}$)	**β-sheet** + Random coil	α-**helix+**β-turn+R. coil	**β-sheet**
WSSYMVHWKNQ	(AChE$_{591-601}$)	**β-sheet** + Random coil	**β-sheet** + Random coil	**β-sheet** + Random coil
YMVHW	(AChE$_{594-598}$)	**β-sheet** + Random coil	β-sheet+β-turn+**R. coil**	β-sheet+β-turn+**R. coil**

FIGURE 2. Secondary structure of T40-IDE peptides. Far UV spectra (250 to 190 nm) before and after pH neutralisation (50 mM NaH$_2$PO$_4$, pH 7.2) of 100 µM T40-IDE peptides. At least three independent assays were performed. (*A*) Representative spectra of the different structures observed. The blue line indicates 0 molar ellipticity. (*B*) Conformation at acidic pH and conformational changes after pH neutralisation for 100 µM T40-IDE peptides. R. coil: random coil. The dominant secondary structure, if any, is in bold. We have used AChE$_{586-599}$ as a benchmark, which is shown in red font.

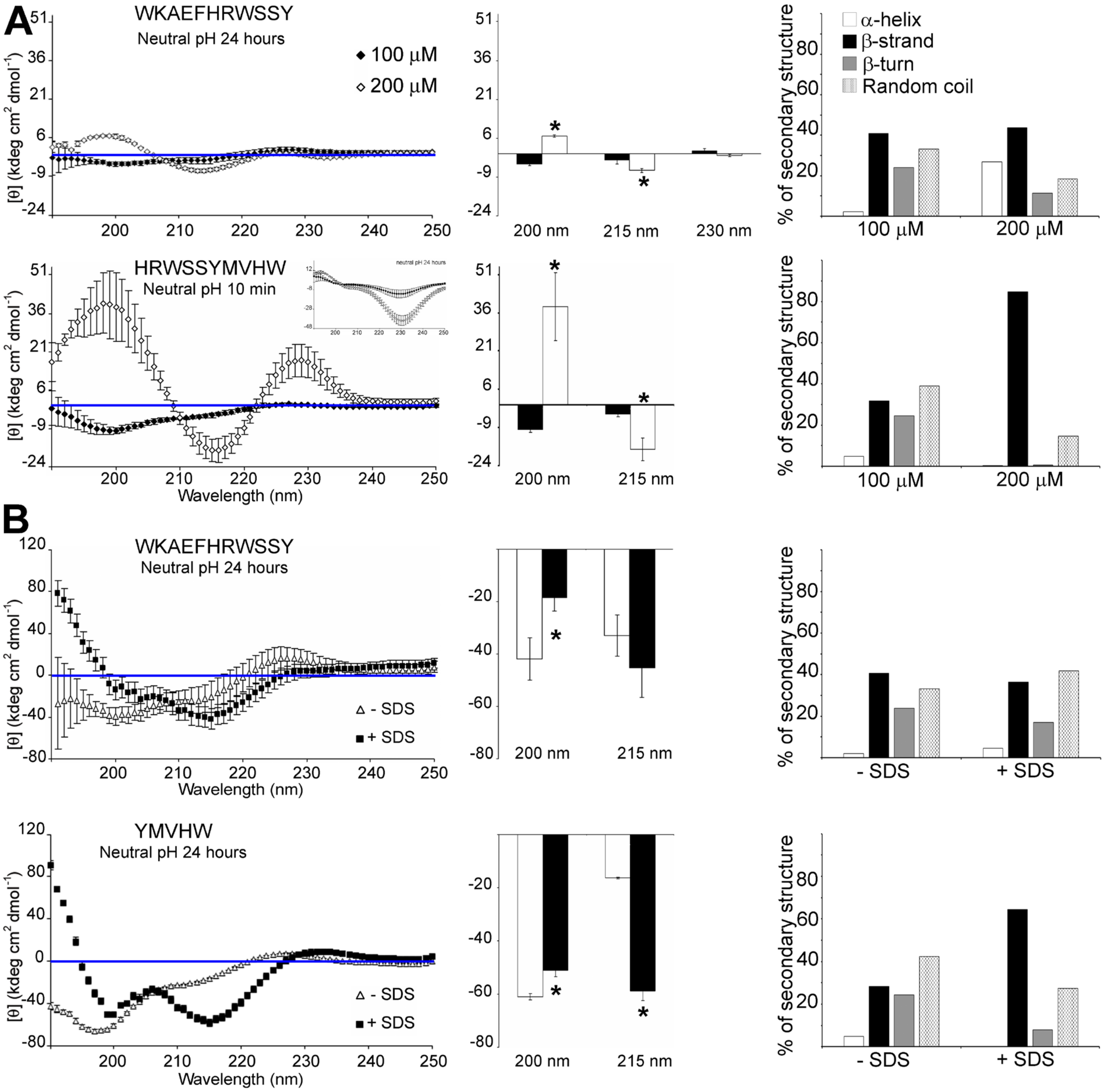

FIGURE 3. Secondary structure of T40-IDE peptides. Far UV spectra (250 to 190 nm) after pH neutralisation (50 mM NaH$_2$PO$_4$, pH 7.2) of 100 and 200 μM AChE$_{584\text{-}594}$ and AChE$_{589\text{-}598}$ (*A*), or 100 μM AChE$_{584\text{-}594}$ and AChE$_{594\text{-}598}$ in absence or presence of 10 mM SDS (*B*). CD spectra (*left panel*) quantification of the signals at 200, 215 and 230 nm (*middle panel*), and percentage of secondary structures (*right panel*). At least three independent assays were performed. The blue line indicates 0 molar ellipticity. * $p<0.03$ when compared to 100 μM peptide (*A*) or without SDS (*B*).

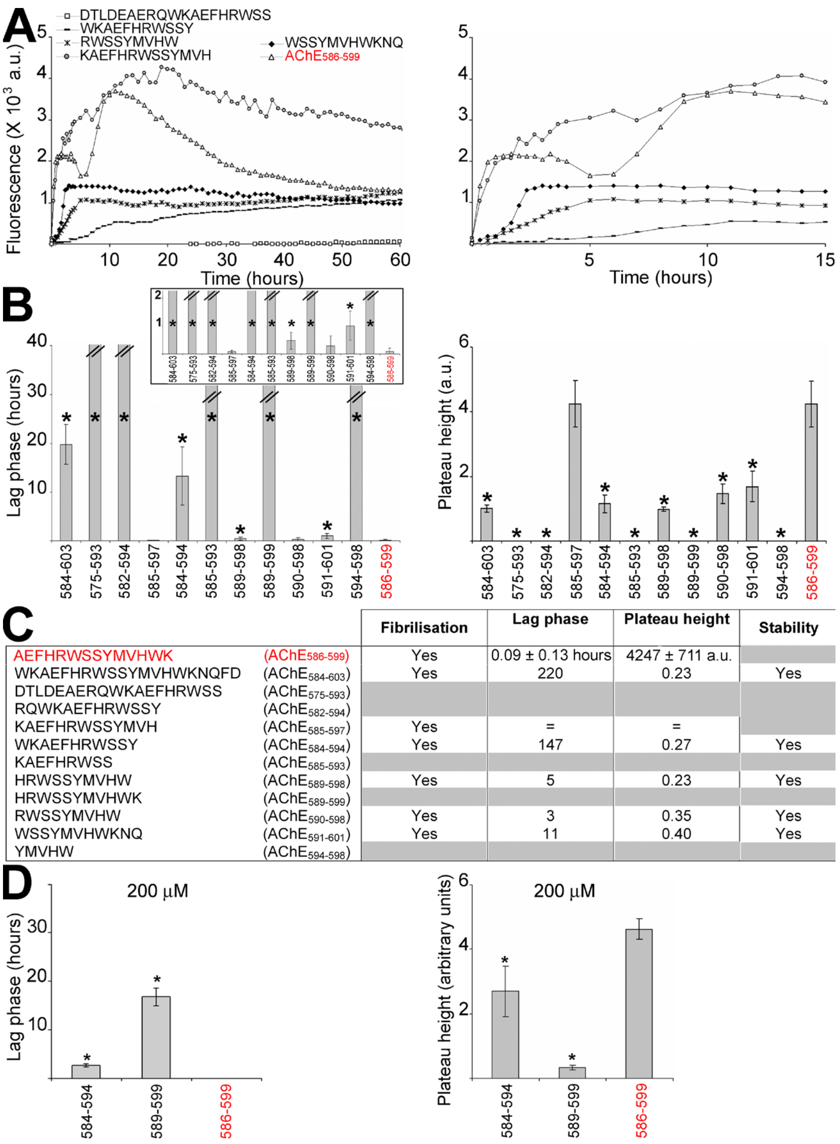

		Fibrilisation	Lag phase	Plateau height	Stability
AEFHRWSSYMVHWK	(AChE586-599)	Yes	0.09 ± 0.13 hours	4247 ± 711 a.u.	
WKAEFHRWSSYMVHWKNQFD	(AChE584-603)	Yes	220	0.23	Yes
DTLDEAERQWKAEFHRWSS	(AChE575-593)				
RQWKAEFHRWSSY	(AChE582-594)				
KAEFHRWSSYMVH	(AChE585-597)	Yes	=	=	
WKAEFHRWSSY	(AChE584-594)	Yes	147	0.27	Yes
KAEFHRWSS	(AChE585-593)				
HRWSSYMVHW	(AChE589-598)	Yes	5	0.23	Yes
HRWSSYMVHWK	(AChE589-599)				
RWSSYMVHW	(AChE590-598)	Yes	3	0.35	Yes
WSSYMVHWKNQ	(AChE591-601)	Yes	11	0.40	Yes
YMVHW	(AChE594-598)				

FIGURE 4. Fibrilisation kinetics of T40-IDE peptides. 100 or 200 µM peptide was incubated with 165 µM ThT in PBS and ThT emission was monitored. At least three independent assays were performed. (*A*) Representatives of the changes in ThT fluorescence observed (the *right panel* is a zoom in of the time scale to visualise the rapid fibrilisation of some peptides). The lag phase of fibrilisation (*B*, *left panel*) and plateau height (*B*, *right panel*) are depicted. * p<0.03 when compared to AChE$_{586\text{-}599}$. The *inset* in *the left panel* represents a zoom up of the y axis of the lag phase. The double bar in *B left panel* indicates the absence of fibrilisation (i.e. an indeterminably long lag phase). (*C*) Summary of the fibrilisation properties for 100 µM of all T40-IDE peptides: ability to fibrilise, duration of lag phase, height of plateau and stability of the amyloid products (indicated by stability or decay of the ThT fluorescence after plateau). The peptides that do not fibrilise and/or the peptides which amyloid products are not stable are indicated by grey boxes. The lag phase and plateau height for the AChE peptides are shown as fold ratio of AChE586-599 (e.g. '=' represents equal value to AChE$_{586\text{-}599}$ and '100' for the lag phase represents 100 times longer than AChE$_{586\text{-}599}$). We have used AChE$_{586\text{-}599}$ as a benchmark, which is shown in red font. (*D*) The lag phase of fibrilisation (*left panel*) and plateau height (*B*, *right panel*) of reactions with 200 µM peptides are depicted. * p<0.04 when compared to AChE$_{586\text{-}599}$. a.u.: arbitrary units.

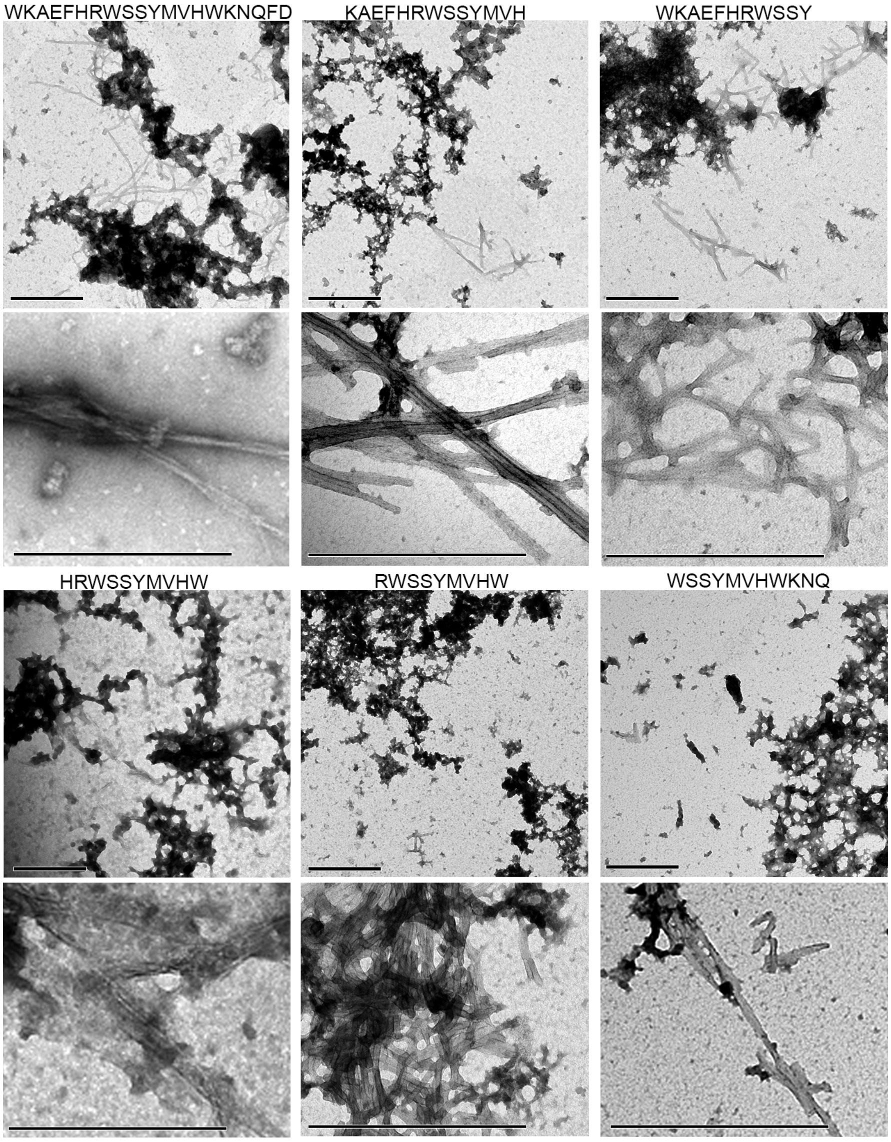

FIGURE 5. Morphology of the fibrilising T40-IDE peptides. 100 μM peptide was incubated with 165 μM ThT in PBS until plateau. Shown are electron micrographs of negatively stained reaction at plateau. The scale bar represents 500 nm.

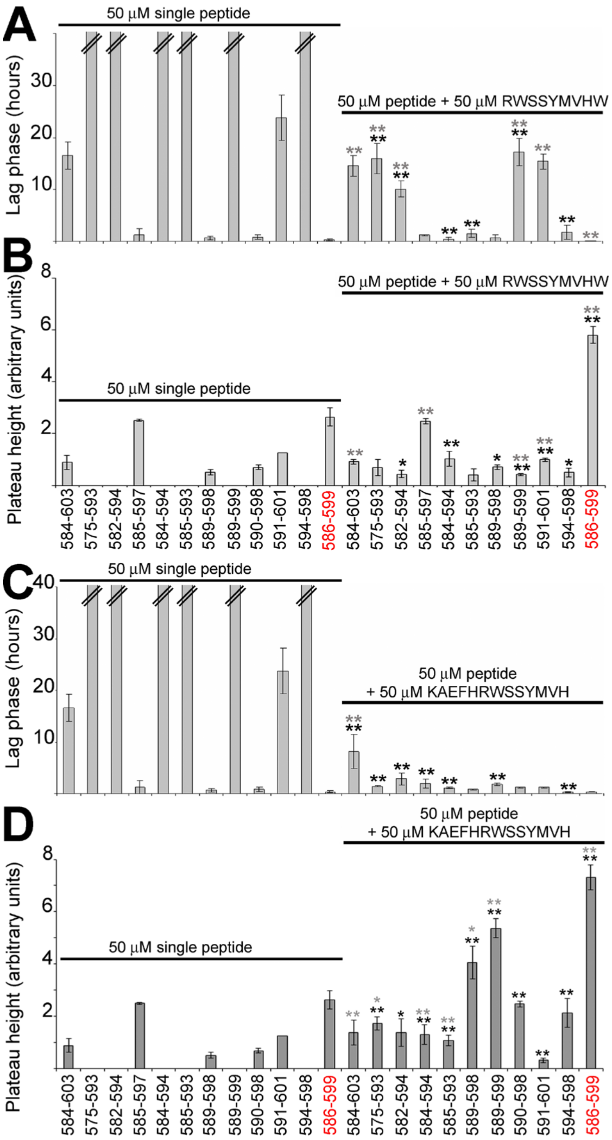

FIGURE 6. Effect of $AChE_{590-598}$ or $AChE_{585-597}$ on T40-IDE peptides and $AChE_{586-599}$ fibrilisation. 50 µM of T40-IDE peptide monomers were incubated with 165 µM ThT in PBS, with or without 50 µM $AChE_{590-598}$ (*A* and *B*) or $AChE_{585-597}$ monomers (*C* and *D*). At least three independent assays were performed. Changes in ThT fluorescence were monitored with the lag phase of fibrilisation (*A* and *C*) and the plateau height (*B* and *D*) depicted. The black '* or **' refers to p values when compared to 50 µM T40-IDE peptide alone, and the grey '* or **' refers to p values when compared to 50 µM $AChE_{590-598}$ or $AChE_{585-597}$ alone. One '*' ' (black or grey) is for $p<0.05$, and two '**' (black or grey) is for $p<0.03$. The double bar in *A* and *C* indicates the absence of fibrilisation (i.e. an indeterminably long lag phase). We have used $AChE_{586-599}$ as a benchmark, which is shown in red font.

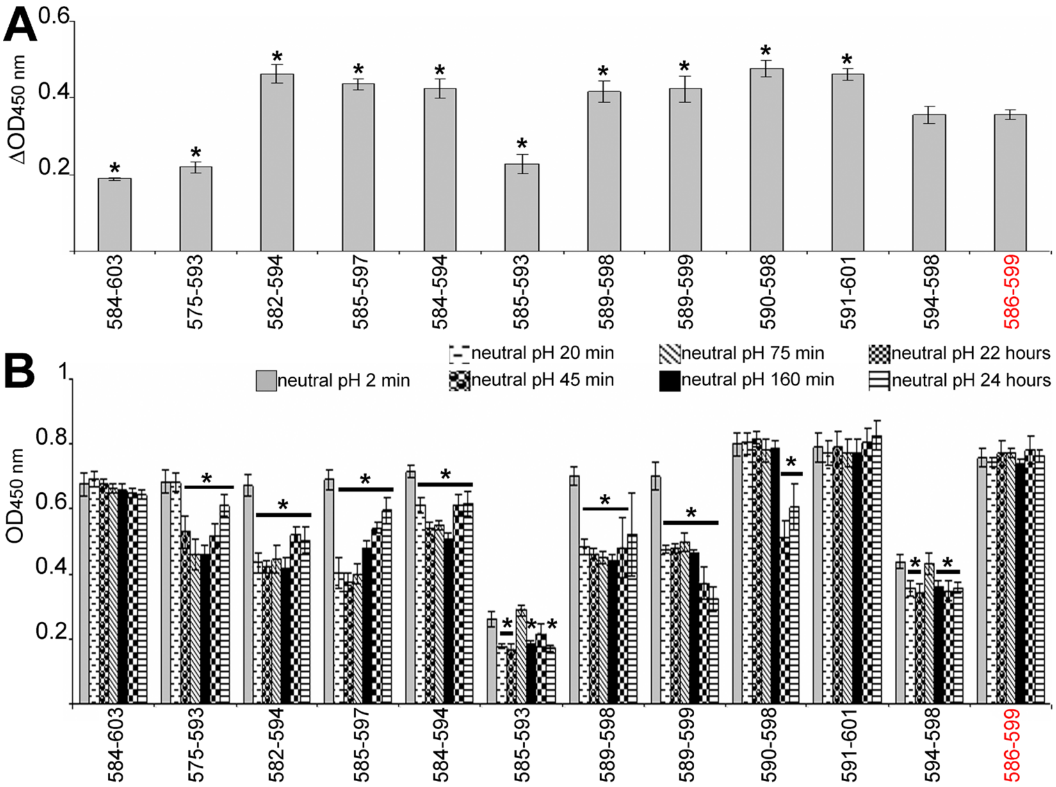

C

		Surfactant activity	Stability
AEFHRWSSYMVHWK	(AChE$_{586-599}$)	1.0 (0.36 ± 0.01 ΔOD)	Yes
WKAEFHRWSSYMVHWKNQFD	(AChE$_{584-603}$)	0.53	Yes
DTLDEAERQWKAEFHRWSS	(AChE$_{575-593}$)	0.62	
RQWKAEFHRWSSY	(AChE$_{582-594}$)	1.30	
KAEFHRWSSYMVH	(AChE$_{585-597}$)	1.23	
WKAEFHRWSSY	(AChE$_{584-594}$)	1.19	
KAEFHRWSS	(AChE$_{585-593}$)	0.64	
HRWSSYMVHW	(AChE$_{589-598}$)	1.17	
HRWSSYMVHWK	(AChE$_{589-599}$)	1.19	
RWSSYMVHW	(AChE$_{590-598}$)	1.34	Yes*
WSSYMVHWKNQ	(AChE$_{591-601}$)	1.30	Yes
YMVHW	(AChE$_{594-598}$)	1.0	

FIGURE 7. Surface activity of the T40-IDE peptides. The surface activity of 50 µM T40-IDE peptides was measured before and after neutralisation (1M NaH_2PO_4, pH 7.2). At least three independent assays were performed. (*A*) Representative surfactant activity of the T40-IDE peptides and AChE$_{586-599}$ 2 min after neutralisation. $\Delta OD = (OD_{offset} - OD_{central})_{neutral\ pH\ 2min} - (OD_{offset} - OD_{central})_{acidic\ pH}$. * $p<0.023$ when compared to AChE$_{586-599}$. (*B*) Temporal pattern of the surface activity for the T40-IDE peptides after neutralisation. $OD = OD_{offset} - OD_{central}$.* $p<0.034$ when compared to the same peptide after 2 min at neutral pH. (*C*) Summary of the surfactant properties for the T40-IDE peptides: surface activity dependent on pH (depicted by subtracting the value at acidic pH to the value at neutral pH after 2 min) and stability of the surface activity (indicated by stability or decay of the OD signal). The peptides with unstable surfactant activity are indicated by grey boxes. '*' indicates peptides which activity remains stable over most of the time course, except two time point. The activity for the T40-IDE peptides is shown as fold ratio of AChE$_{586-599}$ activity (e.g. '1' represents equal value to AChE$_{586-599}$). We have used AChE$_{586-599}$ as a benchmark, which is shown in red font.

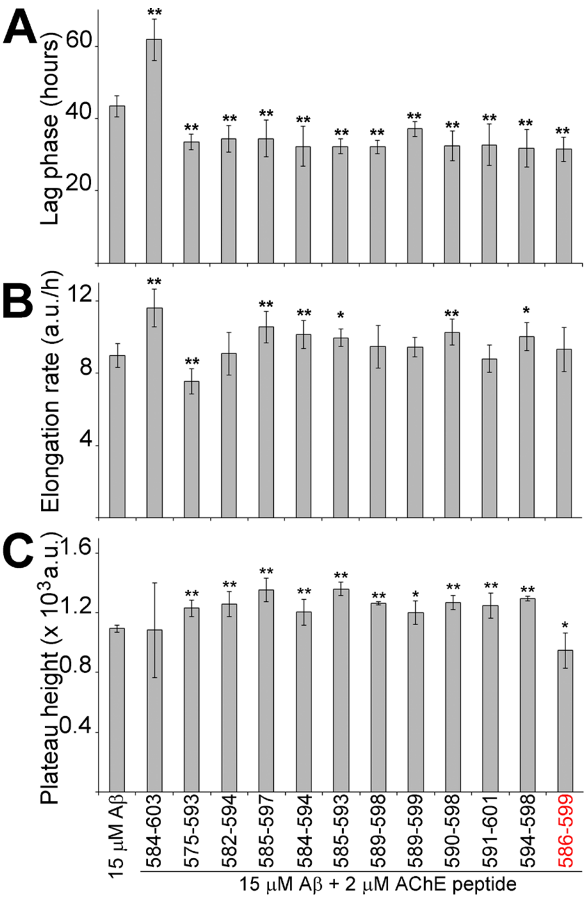

FIGURE 8. T40-IDE peptide seeds promote Aβ fibrilisation. 15 μM Aβ was incubated with 165 μM ThT in PBS, with or without 2 μM T40-IDE peptide seeds, and ThT emission was monitored. At least three independent assays were performed. The lag phase of fibrilisation (*A*), elongation rate (*B*) and plateau height (*C*) are depicted. * $p<0.05$ and ** $p<0.03$ when compared to Aβ without seeds. a.u.: arbitrary units. We have used AChE$_{586\text{-}599}$ as a benchmark, which is shown in red font.

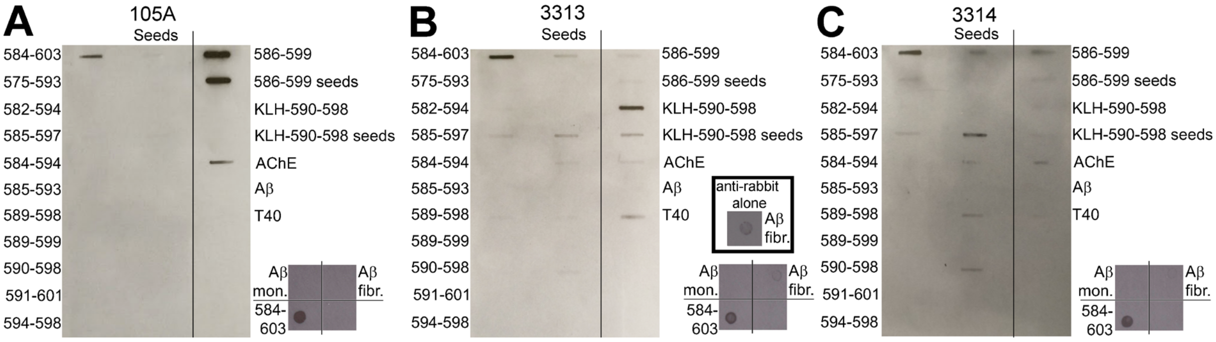

FIGURE 9. Specificity of Mab 105A (*A*) and polyclonal antibodies 3313 (*B*) and 3314 (*C*). T40-IDE peptide or peptide seeds, AChE, Aβ monomers (mon.), Aβ fibrils (fibr.), and T40 were blotted onto a nitrocellulose membrane. Blocking was performed with 0.4% fish skin gelatin before incubation with mouse Mab 105A, or rabbit polyclonal antibody 3313 or 3314, followed by anti-mouse or anti-rabbit IgG conjugated to HRP. Products were visualised by enhanced chemiluminescence. The additional inset in *B* shows the reactivity of the polyclonal secondary antibodies anti-rabbit (no first antibodies were added) against Aβ fibrils under the same conditions.

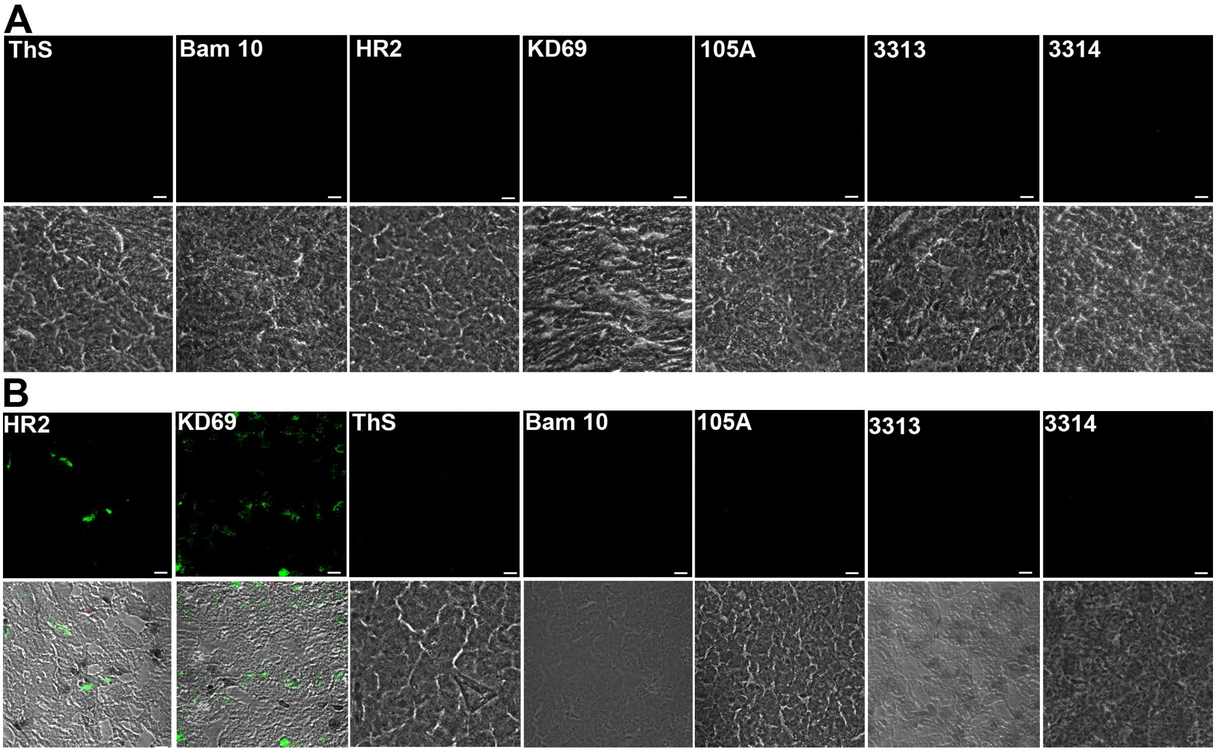

Figure 10. Reactivity of the antibodies in brains of age-matched control and hAChE-S single transgenic mice. (*A*) Absence of reactivity of ThS and the antibodies against Aβ, hAChE-S and AChE peptides in the brain of age-matched control mice. (*B*) In the brain of hAChE-S single transgenic mice, the only reactivity detected is that of the antibodies recognising globular hAChE-S. Frozen brain sections (12 μm) were labelled with the Elite ABC M.O.M. kit or Vectastain Elite ABC rabbit IgG kit using a biotinylated anti-mouse or anti-rabbit secondary antibody and FITC conjugated avidin (Vector). The scale bar represents 10 μm. Shown is one of the z slices from a z stack.

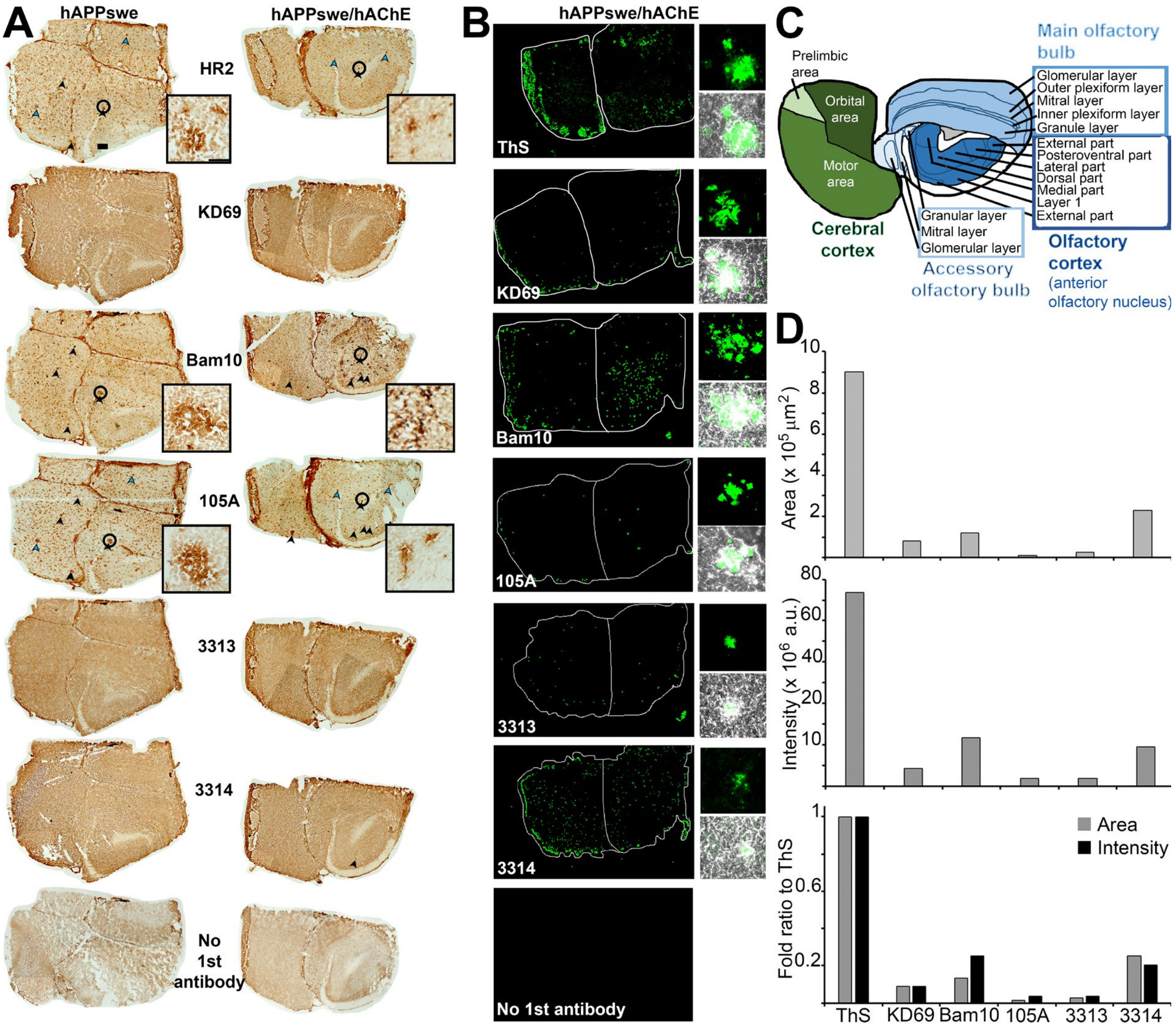

FIGURE 11. Localisation and recognition of mature plaques in the brain of hAPPswe single transgenic (*A, left column*) and hAChE-S/hAPPswe double transgenic mice (*A, right column, and B*). (*A*) Frozen brain sections (12 µm) from single and double transgenic mice were single labelled with the Elite ABC M.O.M. kit or Vectastain Elite ABC rabbit IgG kit using a biotinylated anti-mouse or anti-rabbit secondary antibody, followed by avidin-conjugated peroxidase and then the peroxidase substrate (DAB, Vector). The scale bar represents 200 µm (in the top left brain section). Black arrowheads indicate examples of mature plaques labelled with both anti-Aβ and anti-intact or anti-domains of hAChE-S, whereas blue arrowheads indicate examples of mature plaques labelled only with anti-intact or anti-domains of hAChE-S. The insets show z projections of the same mature plaque (identified by a black circle in the full brain section) labelled with each of the following antibodies, HR2, Bam10 and 105A, and the scale bar represents 50 µm. (*B*) Frozen brain sections (12 µm) from double hAChE-S/hAPPswe transgenic mice were single labelled with the Elite ABC M.O.M. kit or Vectastain Elite ABC rabbit IgG kit using a biotinylated anti-mouse or anti-rabbit secondary antibody and FITC conjugated avidin (Vector). Shown are fluorescent labelling of whole brain sections (*left*) and z projections of mature plaques (fluorescent labelling and merged phase, *right*). (*C*) Mouse brain map at the rostral level, indicating the main brain regions with their sub-areas. (*D*) Shown are quantitation of the area occupied overall by the fluorescent labelling from a specific antibody/reagent in the whole brain section of hAPPswe/hAChE double transgenic (i.e. the whole brain section shown in *B*)(top graph), the overall intensity of the fluorescent labelling in the whole brain section of hAPPswe/hAChE double transgenic (middle graph), and the fold ratio when compared to ThS of each fluorescent labelling in term of area occupied and intensity (bottom graph).

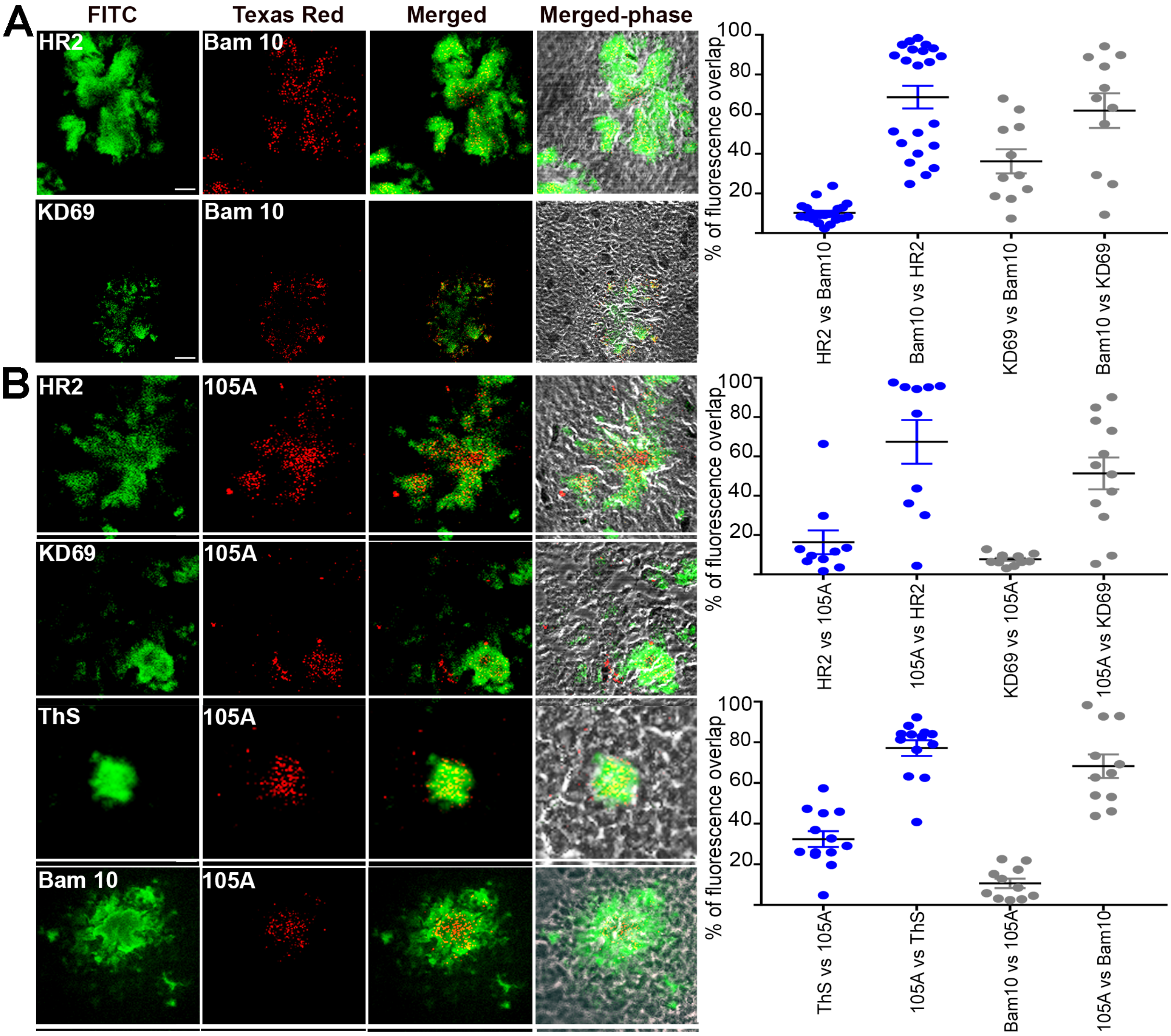

FIGURE 12. Localisation of hAChE-S, T40 (*A*) and β-sheet derived hAChE peptides (*B*) in the brain of hAPPswe single transgenic mice. Frozen brain sections (12 μm) from double transgenic mice were double labelled with the Elite ABC M.O.M. kit or Vectastain Elite ABC rabbit IgG kit using a biotinylated anti-mouse or anti-rabbit secondary antibody and FITC or Texas red conjugated avidin (Vector). The scale bar represents 10 μm. Shown is one of the z slices from a z stack, with the inset showing a z projection. The right panels show quantitation of the percentage of overlap between the two fluorophores within the plaques (e.g. HR2 labelling overlapping with KD69 labelling), with plaques examined from at least two different sections per conditions (with the order of the antibody/reagents have been switched for the staining). Also indicated is the mean and error bars are S.E.M.

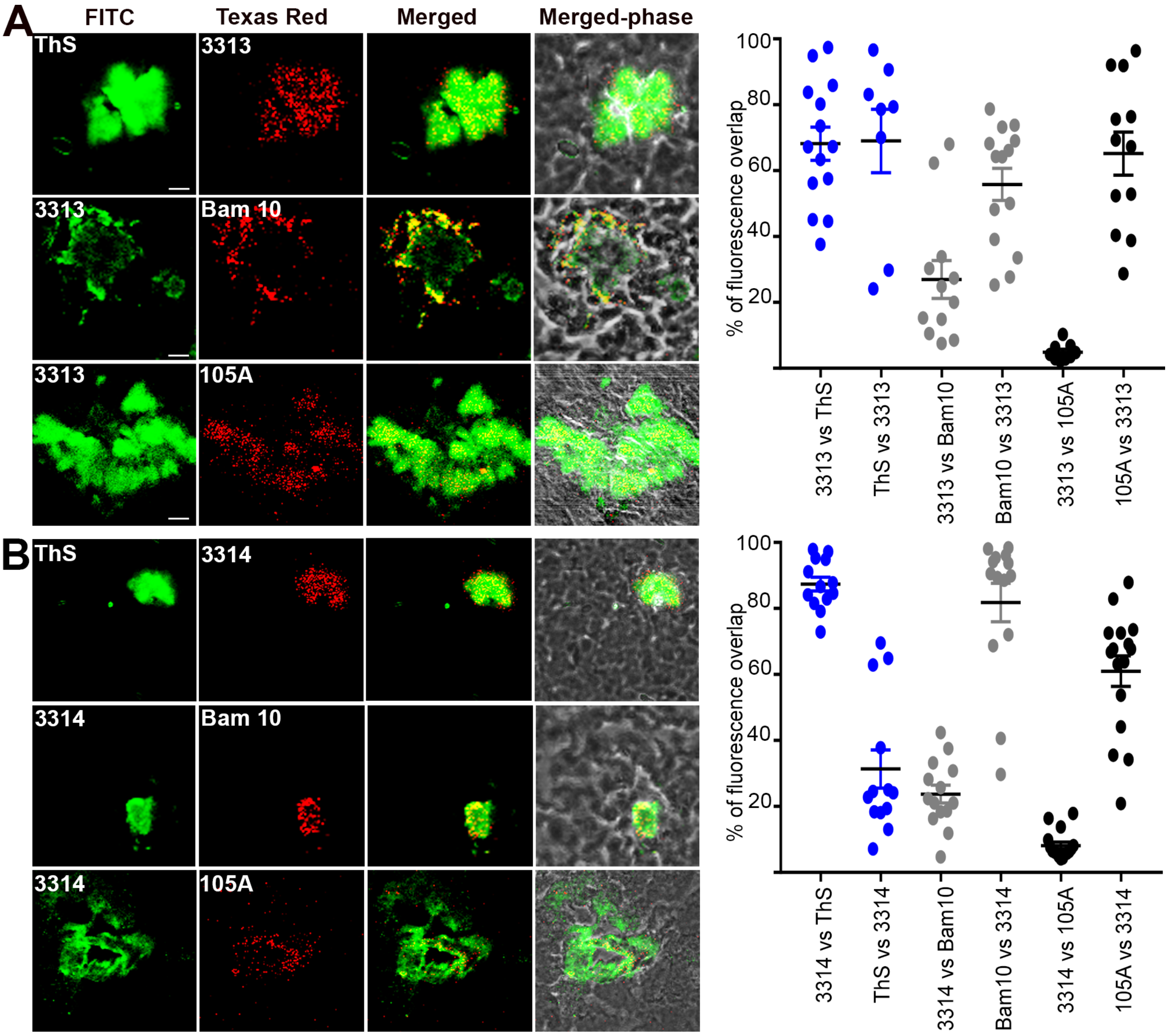

FIGURE 13. Localisation of AChE derived peptides, as recognised by antisera 3313 (*A*) and 3314 (*B*), in the brain of hAPPswe single transgenic mice. Frozen brain sections (12 µm) from single transgenic mice were double labelled with the Elite ABC M.O.M. kit or Vectastain Elite ABC rabbit IgG kit using a biotinylated anti-mouse or anti-rabbit secondary antibody and FITC or Texas red conjugated avidin (Vector). The scale bar represents 10 µm. Shown is one of the z slices from a z stack. The right panels show quantitation of the percentage of overlap between the two fluorophores within the plaques (e.g. ThS labelling overlapping with 3313 labelling), with plaques examined from at least two different sections per conditions (with the order of the antibody/reagents have been switched for the staining). Also indicated is the mean and error bars are S.E.M.

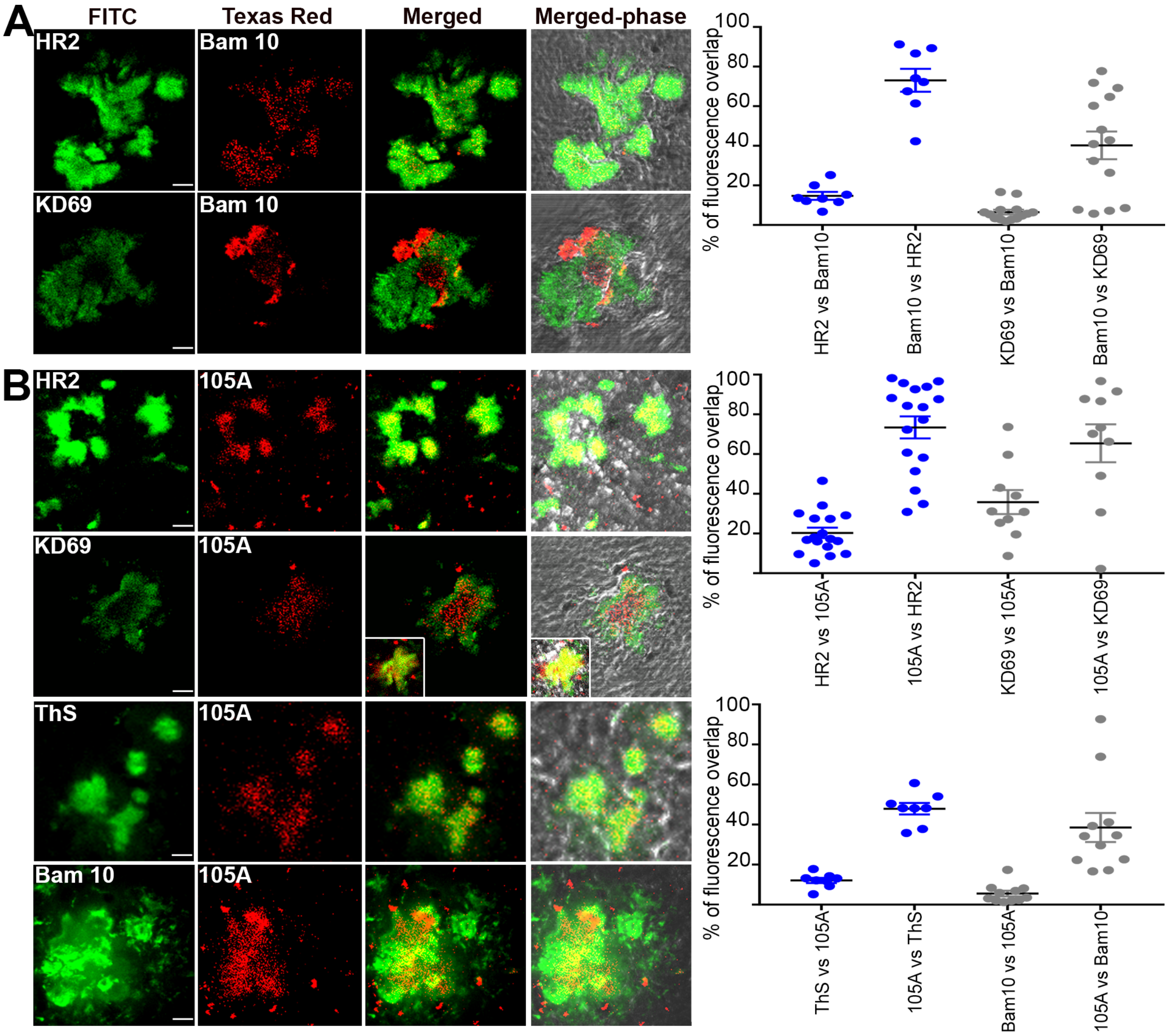

FIGURE 14. Localisation of hAChE-S, T40 (*A*) and β-sheet derived hAChE peptides (*B*) in the brain of hAChE-S/hAPPswe double transgenic mice. Frozen brain sections (12 μm) from double transgenic mice were double labelled with the Elite ABC M.O.M. kit or Vectastain Elite ABC rabbit IgG kit using a biotinylated anti-mouse or anti-rabbit secondary antibody and FITC or Texas red conjugated avidin (Vector). The scale bar represents 10 μm. Shown is one of the z slices from a z stack, with the inset showing a z projection. The right panels show quantitation of the percentage of overlap between the two fluorophores within the plaques (e.g. HR2 labelling overlapping with Bam10 labelling), with plaques examined from at least two different sections per conditions (with the order of the antibody/reagents have been switched for the staining). Also indicated is the mean and error bars are S.E.M.

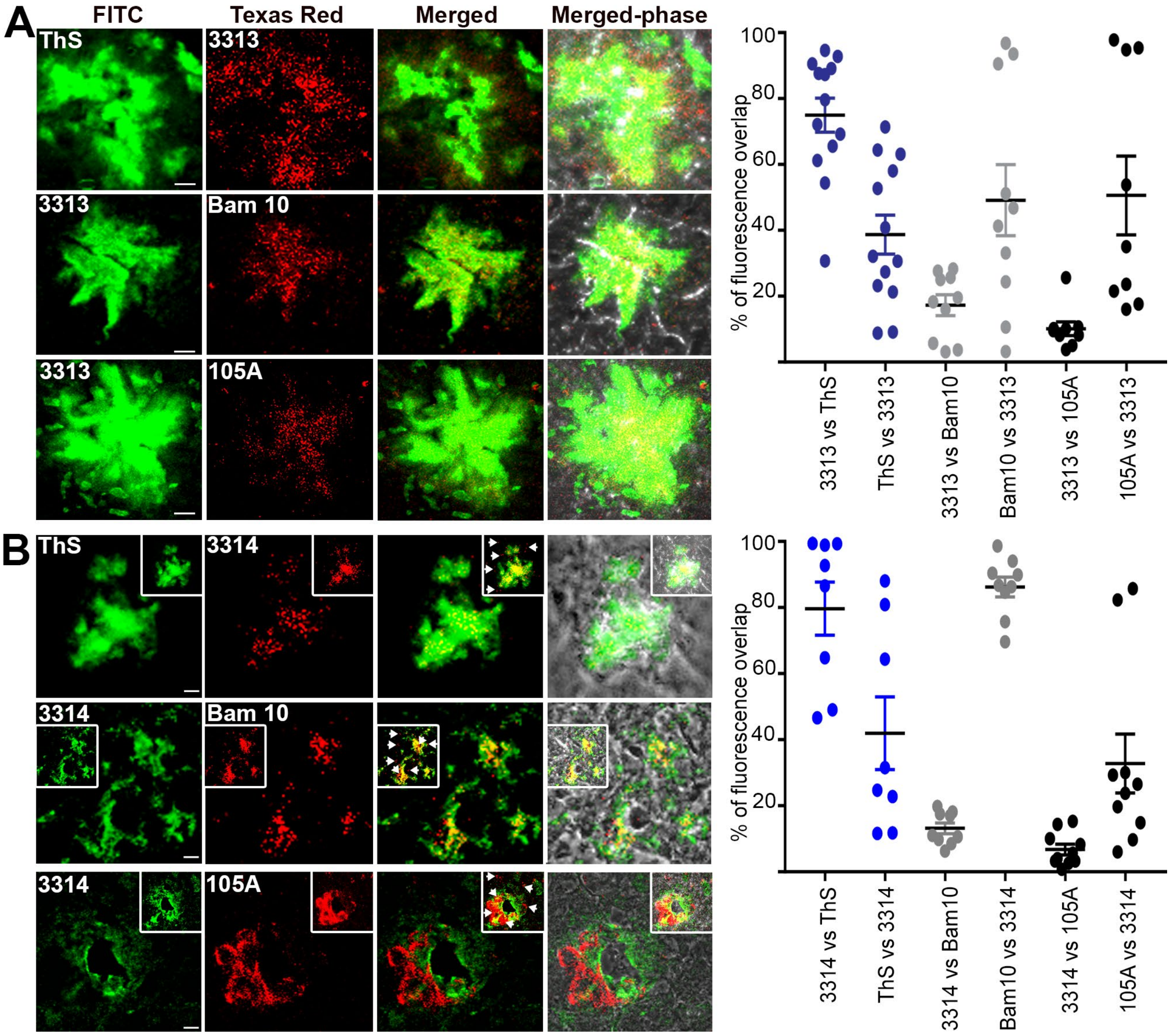

FIGURE 15. Localisation of AChE derived peptides, as recognised by antisera 3313 (*A*) and 3314 (*B*), in the brain of hAChE-S/hAPPswe double transgenic mice. Frozen brain sections (12 µm) from double transgenic mice were double labelled with the Elite ABC M.O.M. kit or Vectastain Elite ABC rabbit IgG kit using a biotinylated anti-mouse or anti-rabbit secondary antibody and FITC or Texas red conjugated avidin (Vector). The scale bar represents 10 µm. Shown is one of the z slices from a z stack, with the insets showing z projections. In (*B*), *arrows* indicate hAChE-S species in discrete and distinct areas from those associated with fibrilar amyloids. The right panels show quantitation of the percentage of overlap between the two fluorophores within the plaques (e.g. ThS labelling overlapping with 3313 labelling), with plaques examined from at least two different sections per conditions (with the order of the antibody/reagents have been switched for the staining). Also indicated is the mean and error bars are S.E.M.